Research and development of a new fine-grained scintillator tracker for the upgrade of T2K near detector

(T2K実験前置検出器アップグレードのための新しい細分割型シンチレータトラッカーの研究開発)

Ryo Fujita
Department of Physics, University of Tokyo

Abstract

The T2K experiment plans to extend the current running aiming at initial observation of the CP violation with 3σ significance. Along with an extension of the T2K running, a program of near detector upgrade is undertaken aiming at reduction of systematic uncertainty down to $\sim$4%.

In the upgrade detector, a new highly granular scintillator target detector, named Super-FGD, will replace the upstream part. Super-FGD will consist of about 2 million cubes with the size of each being $1\times1\times1$ cm^3. This thesis reports the performance evaluation of Super-FGD with several types of small cube units using a positron beam.

Contents

1 Introduction **4**
1.1 Neutrino oscillation . . . 4
1.2 Neutrino-nucleus interaction . . . 5
1.3 The T2K experiment . . . 6
1.3.1 J-PARC neutrino beam . . . 7
1.3.2 Near detector “ND280” . . . 8
1.3.3 Far detector “Super-Kamiokande” . . . 8
1.3.4 Status and prospects of T2K . . . 9
1.4 T2K ND280 Upgrade . . . 10
1.4.1 Design of the upgrade detector . . . 11
1.4.2 Strengths and weaknesses of current ND280 . . . 11
1.4.3 Advantages of the upgrade detector . . . 12
1.4.4 Requirements for the upgrade detector . . . 14
1.5 Contents of this thesis . . . 14

2 Super-FGD **15**
2.1 Introduction . . . 15
2.2 Detector components . . . 16
2.2.1 Plastic scintillator cubes . . . 16
2.2.2 Wavelength shifting fiber . . . 16
2.2.3 Multi-pixel photon counter (MPPC) . . . 17
2.2.4 Readout electronics . . . 17
2.2.5 Optical interface . . . 18
2.2.6 Cube assembly . . . 19
2.3 Current status and tasks of Super-FGD R&D . . . 21

3 Performance evaluation of Super-FGD prototype with a positron beam **22**
3.1 Purpose of the beam test . . . 22
3.2 Experimental setup . . . 22
3.2.1 Beamline . . . 22
3.2.2 Detector setups . . . 23
3.2.3 Hodoscopes . . . 27
3.2.4 Multi-Pixel Photon Counter (MPPC) . . . 27
3.2.5 Readout electronics and data acquisition system . . . 28
3.3 Data taking and gain calibration . . . 30
3.3.1 Trigger configuration . . . 30
3.3.2 Gain calibration . . . 30
3.3.3 Event selection and statistics . . . 32
3.4 Results of the beam test . . . 35

3.4.1 The response in single cube . . . 35
3.4.2 Measurement with welding sheets . . . 38
3.4.3 Comparison between extruded cubes and injected cubes . . . 40
3.4.4 Prototype with 125 (5×5×5) cubes . . . 44

4 Summary and future prospects **51**
4.1 Summary . . . 51
4.2 Future prospects . . . 51

A Dependence for light yield on the number of inserted fibers **54**
A.1 Motivation . . . 54
A.2 Experimental setup . . . 54
A.3 Data taking . . . 56
A.4 Results . . . 57

Chapter 1

Introduction

1.1 Neutrino oscillation

Neutrino is one of the elementary particles which is categorized as neutral leptons and has a spin of 1/2. There exist three types of neutrinos : electron neutrinos(ν_e), muon neutrinos(ν_μ), tau neutrinos(ν_τ) and corresponding antiparticles called anti-neutrinos.

The Standard Model of elementary particle physics assumes that neutrinos have exactly zero mass. However, the evidence of neutrino oscillation, which implied that neutrinos have non-zero mass, was found by the atmospheric neutrino experiment of Super-Kamiokande[1] in 1998 and required a modification to the Standard Model.

Using a unitary transformation, the neutrino flavor and mass eigenstates can be written as

$$|\nu_\alpha\rangle = \sum_i U^*_{\alpha i} |\nu_i\rangle \tag{1.1}$$

$$|\nu_i\rangle = \sum_\alpha U_{\alpha i} |\nu_\alpha\rangle \tag{1.2}$$

where $|\nu_\alpha\rangle$ $(\alpha = e, \mu, \tau)$ is a flavor eigenstate of neutrino and $|\nu_i\rangle$ $(i = 1, 2, 3)$ is a mass eigenstate of neutrino.

$U_{\alpha i}$ is a 3×3 unitary matrix, called the Pontecorvo-Maki-Nakazawa-Sakata Matrix(the PMNS matrix). This matrix gives the mixing of flavor and mass eigenstates and is given as follows:

$$U = \begin{pmatrix} 1 & 0 & 0 \\ 0 & c_{23} & s_{23} \\ 0 & -s_{23} & c_{23} \end{pmatrix} \begin{pmatrix} c_{13} & 0 & s_{13}e^{-i\delta_{CP}} \\ 0 & 1 & 0 \\ -s_{13}e^{-i\delta_{CP}} & 0 & c_{13} \end{pmatrix} \begin{pmatrix} c_{12} & s_{12} & 0 \\ -s_{12} & c_{12} & 0 \\ 0 & 0 & 1 \end{pmatrix} \tag{1.3}$$

where $c_{ij} = \cos\theta_{ij}$, $s_{ij} = \sin\theta_{ij}$, θ_{ij} is a mixing angle and δ_{CP} is the CP-violating phase. Assuming that ν_α with the energy E is detected as ν_β after propagation for a distance L, the probability of neutrino oscillation is expressed as

$$\begin{aligned} P(\nu_\alpha \to \nu_\beta) = \delta_{\alpha\beta} &- 4\sum_{i>j} Re(U^*_{\alpha i} U_{\beta i} U_{\alpha j} U^*_{\beta j}) \sin^2\left(\frac{\Delta m^2_{ij} L}{4E}\right) \\ &+ 2\sum_{i>j} Im(U^*_{\alpha i} U_{\beta i} U_{\alpha j} U^*_{\beta j}) \sin\left(\frac{\Delta m^2_{ij} L}{2E}\right) \end{aligned} \tag{1.4}$$

where $\Delta m_{ij}^2 = m_i^2 - m_j^2$ are differences in the squares of eigenmasses. The existence of neutrino oscillation indicates that Δm_{ij}^2 is a non-zero value.
The probability of electron neutrino appearance is approximately given by

$$P(\nu_\mu \to \nu_e) \simeq \sin^2\theta_{23}\sin^2 2\theta_{13}\sin^2\left(\frac{1.27\ \Delta m_{13}^2[\mathrm{eV}^2]\ L[\mathrm{km}]}{E[\mathrm{GeV}]}\right). \tag{1.5}$$

In the PMNS matrix, a CP-violating phase exists. The effect of CP-violating phase appears in the difference of $\nu_\mu \to \nu_e$ and $\bar{\nu}_\mu \to \bar{\nu}_e$ appearance probabilities as

$$\begin{aligned} P(\nu_\mu \to \nu_e) - P(\bar{\nu}_\mu \to \bar{\nu}_e) = &-2\sin\delta_{CP}\cos\theta_{13}\sin 2\theta_{12}\sin 2\theta_{13}\sin 2\theta_{23} \\ &\times \sin^2\left(\frac{\Delta m_{32}^2 L}{4E}\right)\sin^2\left(\frac{\Delta m_{31}^2 L}{4E}\right)\sin^2\left(\frac{\Delta m_{21}^2 L}{4E}\right) \end{aligned} \tag{1.6}$$

The search for CP violation in the lepton sector is one of the important work for long baseline neutrino experiment.

1.2 Neutrino-nucleus interaction

Neutrino-nucleus interactions are categorized into charged current and neutral current interactions. Neutrino cross section in differrent interaction modes are shown in Fig.1.1.

In the T2K experiment, a chraged current quasi elastic (CCQE) interaction is a main interaction in the T2K energy range because energy of an initial neutrino can be reconstructed as a two-body interaction by using only the outgoing charged lepton kinematics, assuming that the target nucleon is at rest. The process of CCQE is written as:

$$\nu_l + n \to l^- + p, \tag{1.7}$$

$$\bar{\nu}_l + p \to l^+ + n, \tag{1.8}$$

where a charged lepton $l(=e, \mu, \tau)$ and a nucleon are produced in the interaction between a(n) neutrino (anti-neutrino) and a nucleon in the target.

Other charged current modes, which are background to CCQE, are suppressed by using neutrinos with energy less than 1 GeV.

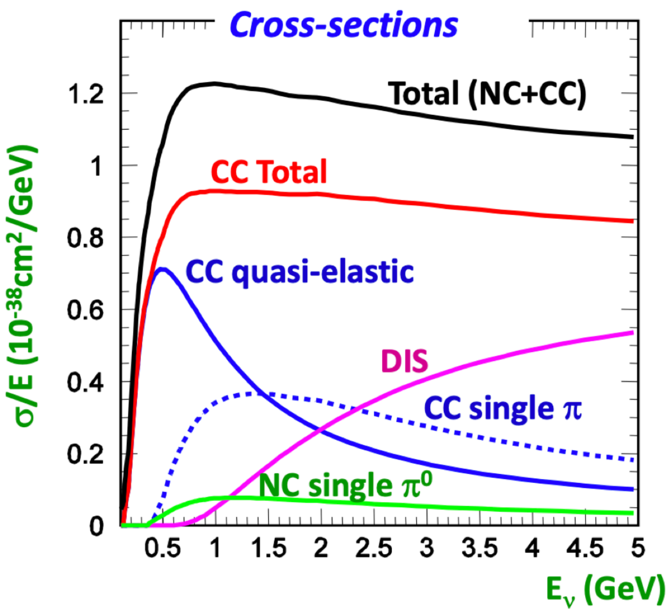

Figure 1.1: Neutrino cross sections[2]

On the other hand, the 2p-2h interaction, which resembles the CCQE in final state, is one of the cause of uncertainty in neutrino-nucleus interaction for the T2K experiment. A pion exchanged by the nucleons in the target nucleus gives two nucleons in the final state. It is difficult to observe this interaction directly with the current ND280 because several hundred MeV of low momentum protons in the final state is lower than the momentum threshold in the current ND280[4]. However, the theoretical model of 2p-2h needs to be constrained by estimating cross section because it is important for measurements of neutrino oscillation parameters to reconstruct neutrino energy precisely.

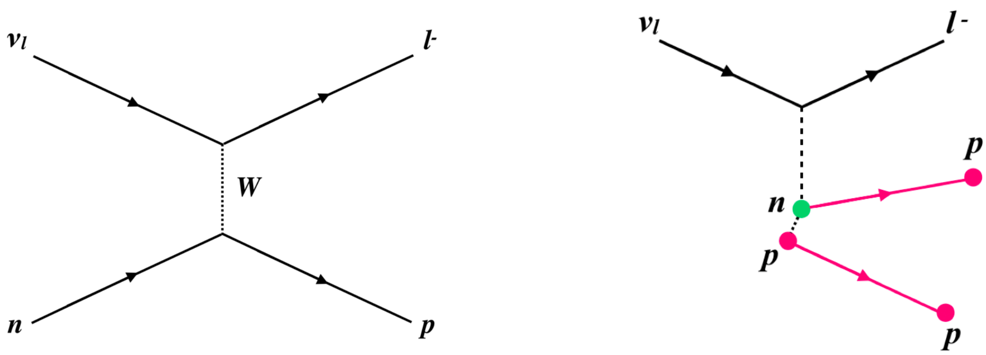

Figure 1.2: Diagrams of CCQE (left) and 2p-2h (right)

1.3 The T2K experiment

The T2K (Tokai to Kamioka) experiment is a long baseline neutrino experiment in Japan[3]. $\nu_\mu(\bar{\nu}_\mu)$ beam produced at Japan Proton Accelerator Research Complex(J-PARC) in Tokai village is measured by a near detector(ND280) and a far detector(Super-Kamiokande, SK). ND280 is located in 280 m downstream from the beam target and SK in 295 km downstream. One of the goals of T2K is precision measurements of oscillation parameters $\theta_{13}, \theta_{23}, \Delta m^2_{32}$ in $\nu_\mu \to \nu_e$ ($\bar{\nu}_\mu \to \bar{\nu}_e$) appearance and $\nu_\mu \to \nu_\mu$ ($\bar{\nu}_\mu \to \bar{\nu}_\mu$) disappearance.

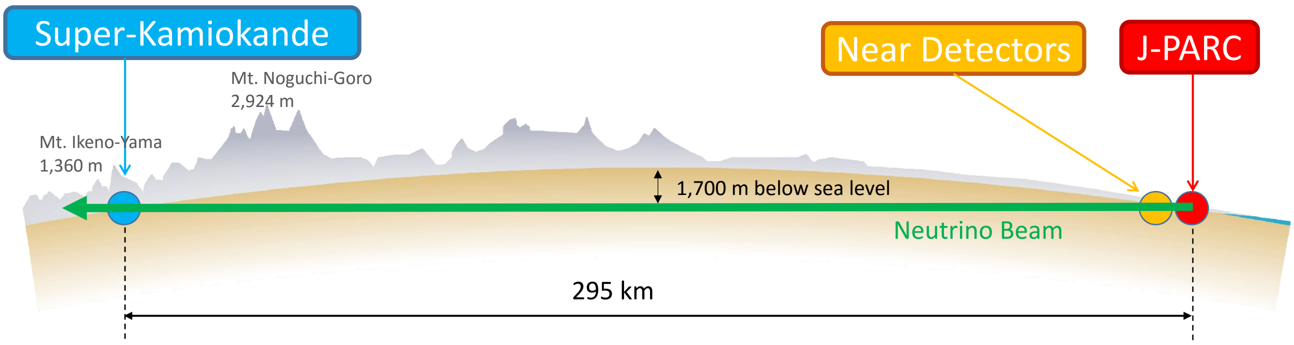

Figure 1.3: The overview of the T2K experiment

1.3.1 J-PARC neutrino beam

J-PARC has three accelerators, a linear accelerator (LINAC), a rapid-cycling synchrotron (RCS), and a main ring (MR) synchrotron. The proton beam produced in LINAC is accelerated with RCS and MR up to 30 GeV. Each beam spill delivered to the neutrino beamline every 2.48 seconds consists of eight bunches. The beam impinges on a graphite target to produce secondary pions which are focused in parallel by three magnetic horns. The pion decays into a muon and muon-neutrino in the decay volume:

$$\pi^+ \to \mu^+ + \nu_\mu, \tag{1.9}$$
$$\pi^- \to \mu^- + \bar{\nu}_\mu. \tag{1.10}$$

Neutrino or anti-neutrino can be selected by changing polarity of the horn current. Residual hadrons are stopped by the beam dump. On the other hand, the produced neutrinos penetrate through the dump and are measured by the detectors. High-energy muons also penetrate through the dump and are monitored by MUMON which monitors beam direction bunch-by-bunch.

T2K adopts off-axis method which obtains narrow neutrino energy spectrum by locating the detectors out of the beam axis. The 2.5° off-axis angle is adopted in T2K and gives 0.5-0.7 GeV neutrino energy band as shown in Fig.1.5. This angle is optimized in order to maximize the neutrino oscillation probability for a baseline of 295 km.

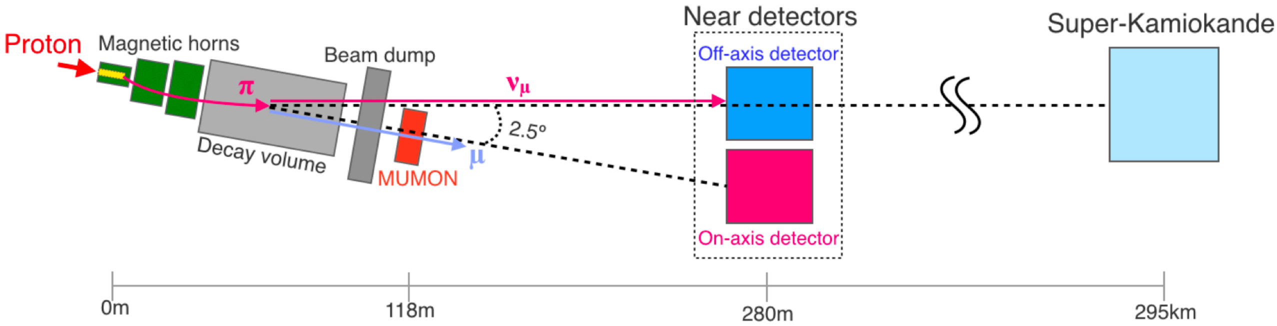

Figure 1.4: The T2K experiment beamline

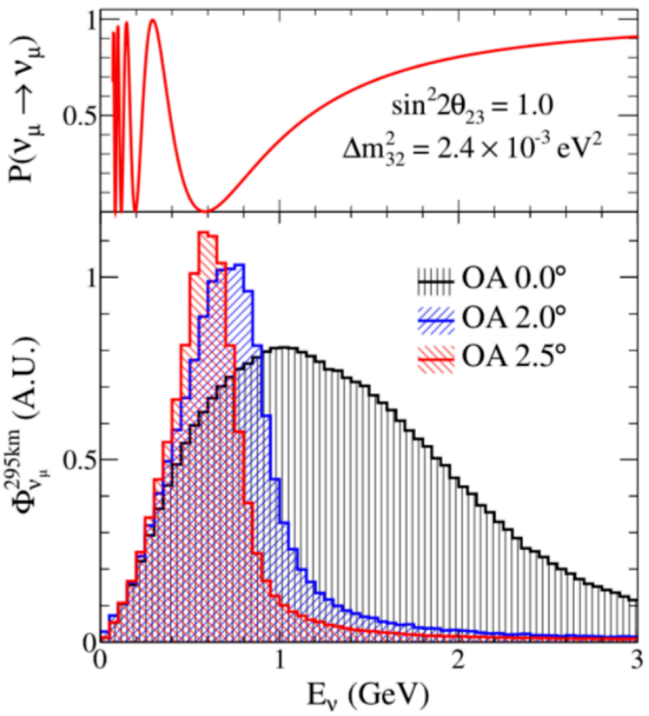

Figure 1.5: Oscillation probability (top) and the relationship between off-axis angles and neutrino energy spectrum (bottom)[5]

1.3.2 Near detector "ND280"

The ND280 is the group of off-axis detectors which measure neutrino interaction before oscillation at 280m downstream from the graphite target. The detectors composing the ND280 is inside the magnet. Two fine-grained detectors (FGDs, upstream one is FGD 1 and downstream one is FGD 2) consisting of square-shaped scintillating bars are the main neutrino target.

1.3.3 Far detector "Super-Kamiokande"

SK is the 50 kt pure water Cherenkov detector which measures neutrino interactions with Cherenkov lights emitted by charged leptons. SK consists of a cylindrical steel tank which is 39m in diameter, 41m in height and a large number of photomultiplier tubes (PMT) covering inside the inner tank.

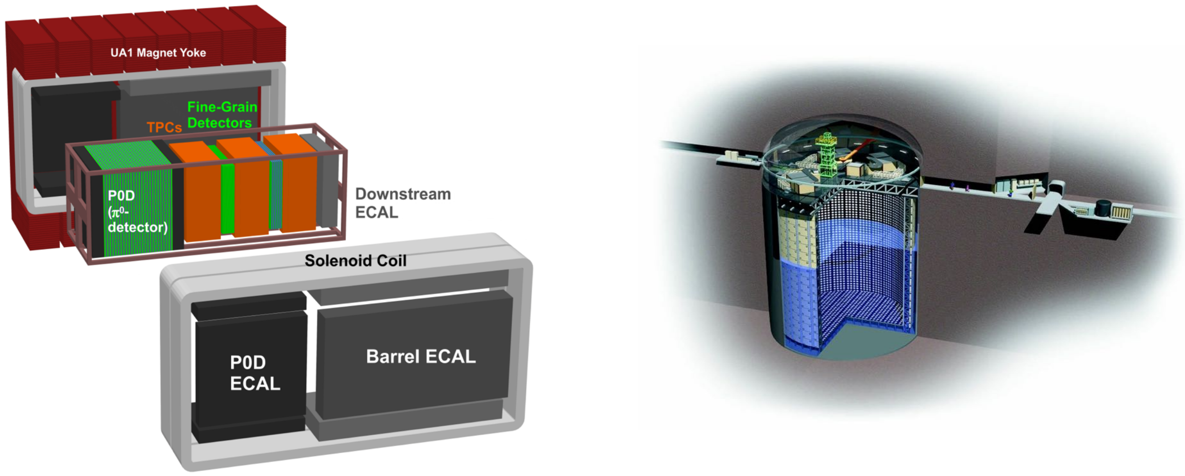

Figure 1.6: The views of ND280 (left) and SK (right) [6][7]

1.3.4 Status and prospects of T2K

The T2K experiment started its physics run in 2010 and the beam power has gradually increased. The total accumulated POT (protons on target) reached 3.16×10^{21} POT with 485kW beam power as of May 2018. This value is equivalent to about 40% of the final goal for T2K. The accumulated data by that time indicates CP violation with 95% C.L. Furthermore, an extension to the current T2K running (T2K-II) is proposed aiming at the observaton of CP violation with 3σ significance[8]. In order to attain this goal, 20×10^{21} POT is accumulated with an increase of the beam power up to 1.3 MW. It is not only important to obtain large statistics but also to reduce systematic uncertainty by better understanding of neutrino flux and interaction.

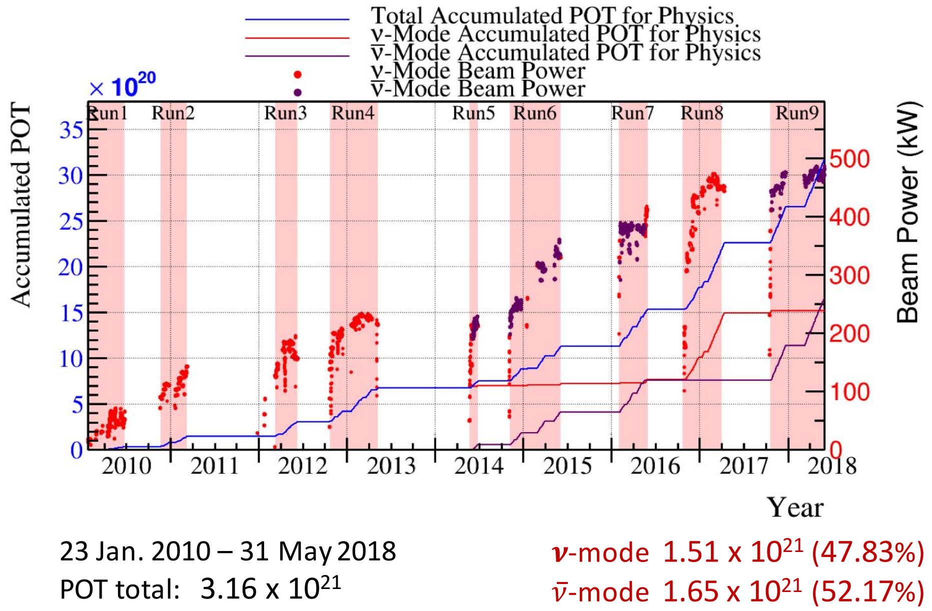

Figure 1.7: Total POT accumulation and MR beam power history

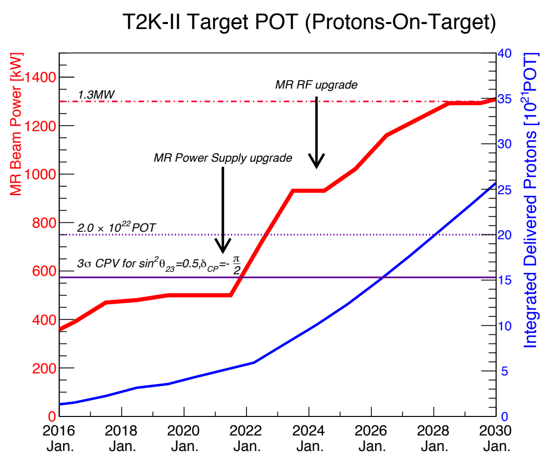

Figure 1.8: Anticipated MR beam power and total POT accumulation until 2030

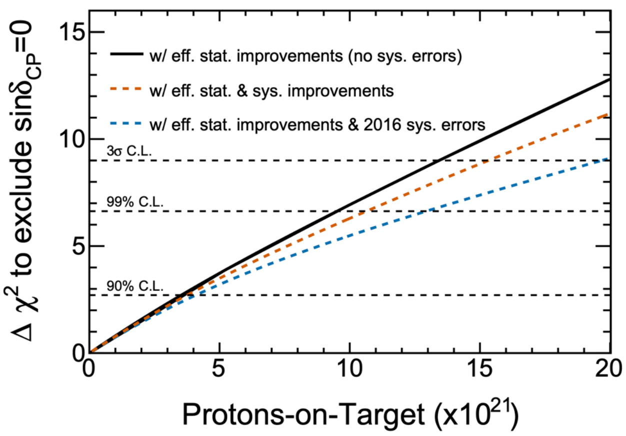

Figure 1.9: Sensitivity to CP violation as a function of POT assuming that the T2K-II data is accumulated in roughly equal periods of ν and $\bar{\nu}$ mode

1.4 T2K ND280 Upgrade

In addition to T2K-II project, a program of near detector upgrade is undertaken aiming at reduction of statistical and systematic uncertainties. The present configuration of T2K gives $\sim 6\%$ systematic errors, and the goal of the upgrade is to reduce it to $\sim 4\%$. This program plans to improve parformance of ND280 by reconfiguring and adding a new fine-grained target detector and two high-angle time projection chambers (HA-TPC). These detectors achieve higher granularity and larger angular acceptance aiming at constraint on the neutrino interaction cross sections.

1.4.1 Design of the upgrade detector

The present ND280 consists of the π^0 detector (P0D), the two fine-grained detectors sandwiched by the three TPCs in the upstream order and 3 types of ECALs are located to surround them as shown in Fig.1.6. The new detector design modifies only in the upstream part except for the upstream ECAL. The new upstream part of ND280 is a sandwich of a high granularity scintillator target detector, which is called Super-FGD[9], with two HA-TPC above and below. This sandwich of detectors is surrounded by six Time-of-Flight (TOF) layers.

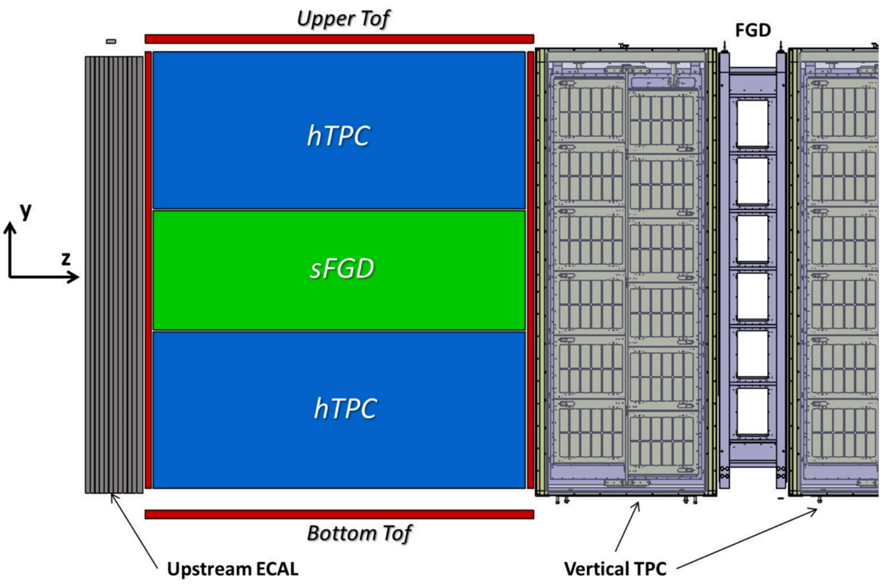

Figure 1.10: The overview of the new detector part for the upgrade

1.4.2 Strengths and weaknesses of current ND280

One of the strength of current ND280 is the performance to measure momentum and charge of leptons produced by neutrino interactions, which makes it possible to distinguish between neutrinos and anti-neutrinos. ND280 also has capacity of particle identification in particular between electrons and muons.

On the other hand, the main weakness of the current design is the low detection efficiency for scattering angles larger than $\sim 40°$ to the beam direction, whereas that in the forward region is quite high. This limitation is caused by the vertical sandwich configuration of FGDs and TPCs to the beam direction.

Another weakness is low efficiency of electron neutrino interactions less than 1 GeV which is caused by limitation of high angle acceptance and contamination of converted gammas. Even if additional statistics is accumulated, this background will constrain systematic uncertainty.

The current ND280 design achieves to obtain good data of muon neutrino interactions and reduce the uncertainties. The upgraded detector will need to select high angle and low energy events with more statistics in T2K-II.

1.4.3 Advantages of the upgrade detector

The current FGD consists of scintillator bars aligned perpendicularly layer-by-layer, while Super-FGD has a cube-stacked structure as shown in Fig. 1.11. Figure 1.12 shows an estimation of the shortest track from one plane in each tracker when a neutrino interaction occurs in the scintillator. A track requires at least three hits in one readout direction. Assuming that the X readout plane is focused on, the shortest track in FGD is estimated at about 4-5 cm long because the plane has a Y readout scintillator bar every two layers. On the other hand, the shortest track in Super-FGD is estimated at about 2-3 cm long thanks to its granular structure. Moreover, 3D readout for Super-FGD is expected to improve a track reconstruction efficiency for protons with low momentum and high scattering angle from a detector simulation as shown in Fig. 1.13. This performance can allow to distinguish between CCQE and 2p-2h.

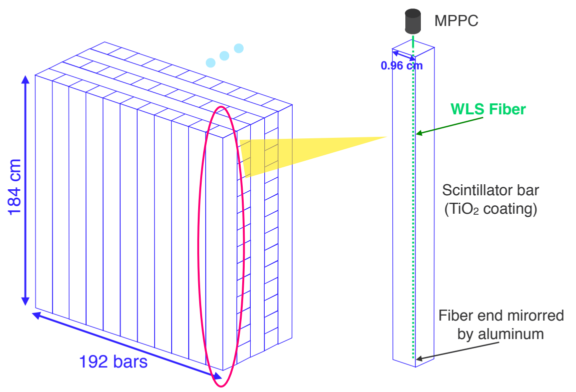

(a) The current FGD

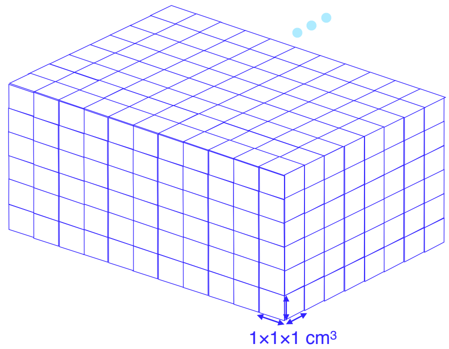

(b) Super-FGD

Figure 1.11: Rough structures of the trackers

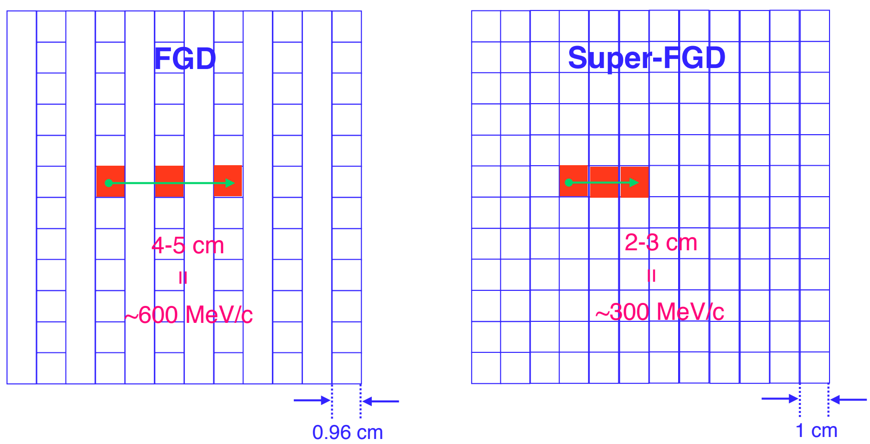

Figure 1.12: Schematic of the shortest tracks in each tracker

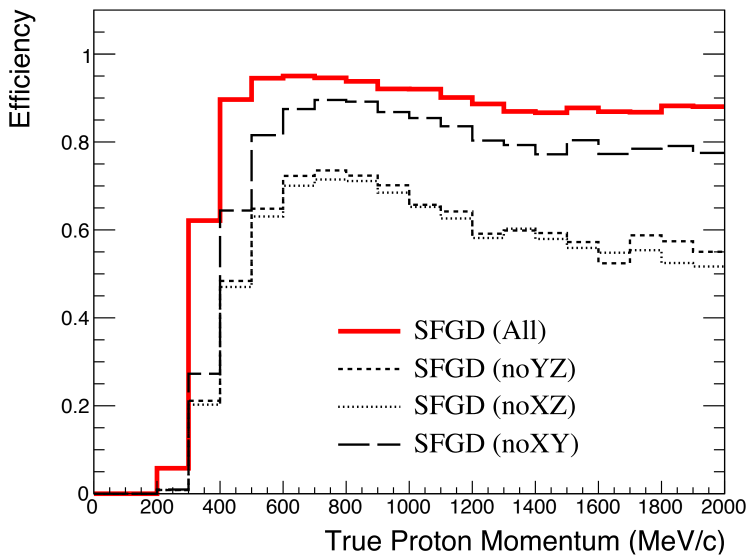

Figure 1.13: Track reconstruction efficiency for protons in Super-FGD. The efficiency around 300-400 MeV/c increases from about 30% to 60% by using channels in all three readout direction.

The upgrade detector improves an efficiency for muons with high scattering angle. Figure. 1.14 shows a simulation result of the event selection efficiency as a function of the muon polar angle for each tracker. It is difficult for the current FGDs to reconstruct muons scattered vertically due to its bar-stacked structure. On the other hand, the efficiency in the upgrade detector for vertical($\cos\theta \simeq 0$) and backward($\cos\theta \simeq$ -1) tracks is expected to increase by about 40% thanks to its 4π acceptance.

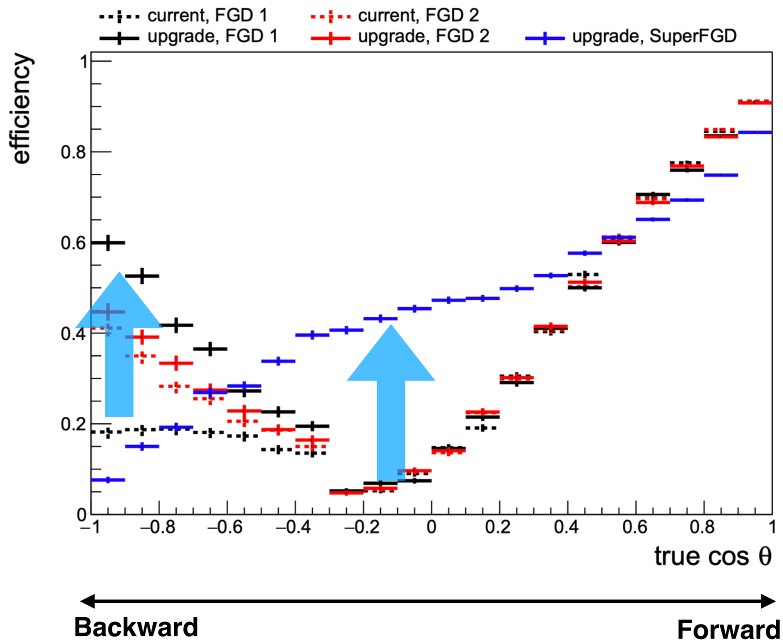

Figure 1.14: Event selection efficiency as a function of the muon polar angle for both the current ND280(dashed lines) and the upgrade detector(solid lines). The different curves correspond to the positions of interaction vertexes in FGD 1 (black), FGD 2 (red) and Super-FGD(blue).

1.4.4 Requirements for the upgrade detector

In order to address the limitations in the previous section, the upgrade detector is required following capabilities:

- High efficiency 4π acceptance for the muons produced in charged current interactions, as well as the low energy pions and protons
- Fiducial mass of a few tons for all targets
- T0 (the time at the production of charged particles) determination of 0.5 ns level in order to determine their direction

1.5 Contents of this thesis

As shown in section 1.4.1, a new scintillator target, named Super-FGD, will be added in the upgrade detector in order to reduce systematic uncertainty in the neutrino oscillation analysis by achieving high granularity and 4π acceptance. R&D of Super-FGD is ongoing to evaluate the performance. The construction of the upgrade detector is expected in 2019-2020, followed by installation and commissioning in 2021.

In this thesis, R&D of Super-FGD and performance evaluation of its prototype are described. The design and components are described in chapter 2. Chapter 3 describes performance evaluation of the Super-FGD components with the positron beam in November 2018 at the research center for ELectron PHoton science (ELPH), Tohoku University.

Chapter 2

Super-FGD

2.1 Introduction

As shown in the previous chapter, the ND280 upgrade adopted Super-FGD as a new scintillator target detector. Fig.2.1 shows the structure and main parameters of the Super-FGD. It consists of 2,064,384 ($192\times192\times56$) plastic scintillator cubes and wavelength shifting (WLS) fibers along three orthogonal directions. Total fiber length is about 62 km. The entire size of Super-FGD is $192\times192\times56$ cm^3 because each scintillator cube is $1\times1\times1$ cm^3. A scintillator cube has three cylindrical holes along x, y and z direction where WLS fibers are inserted. Optical signals from cubes are converted into electrical ones by MPPCs attached to one end of WLS fibers. The number of readout channels is 58,368. Three dimensional readouts make it possible to provide more precise projections of charged particle tracks compared to the current FGDs.

Super-FGD will have roles of the target and the tracker for the neutrino interactions. The detector will have the following characteristics:

- Large mass to provide a sufficient number of the neutrino interactions compared to total mass of the current FGDs
- 4π acceptance for charged leptons with large scattering angle from the charged current interactions
- Capability to identify short tracks of low momentum hadrons

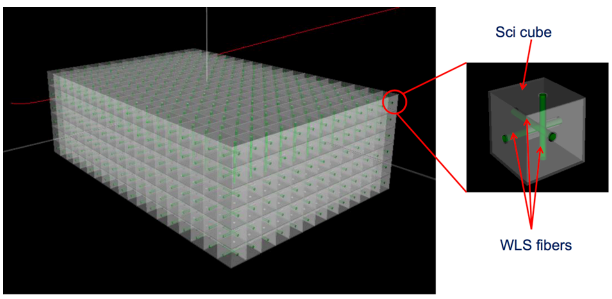

Parameter	Value
# of cubes	2,064,384
# of channels	58,368
Total fiber length	$\sim$ 62 km

Figure 2.1: Structure and main parameters of the Super-FGD[10]

2.2 Detector components

2.2.1 Plastic scintillator cubes

The scintillator cubes are produced at UNIPLAST corporation, in Russia. The cube is composed by mainly polystyrene, 1.5% of paraterphenyl (PTP) and 0.01% of POPOP. A reflecting layer covers the cube by chemical etching. Three cylindrical holes with 1.5 mm diameters are drilled in the cubes. Thickness of a reflector layer was measured with a microscope to be about 90-120 μm.

At the initial stage of R&D, the cubes were produced by extrusion. In this method, a scintillator melts into a liquid which is forced through a die to form a long bar sized 1×1 cm^2 in cross section and cut into cubes. On the other hand, another production method called injection molding is planned to be adopted for the final detector. A melted scintillator is injected into a mold cavity where it cools and hardens to cubic shape. The reasons why the latter is adopted are mainly the reproducibility.

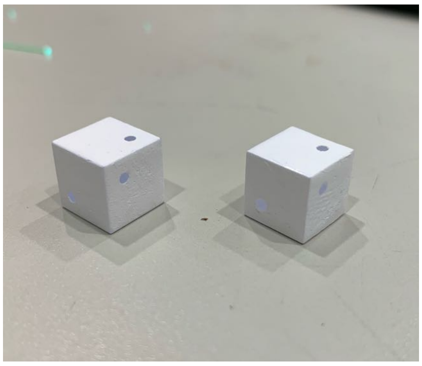

(a) An injected cube (left) and an extruded cube (right)

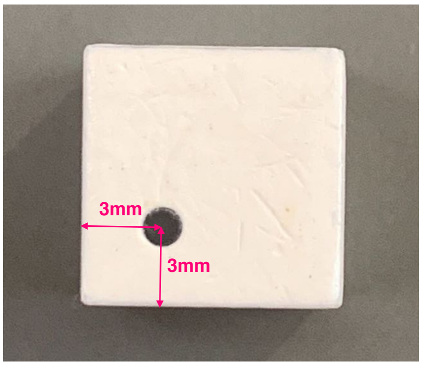

(b) Fiber hole position

Figure 2.2: The scintillator cubes

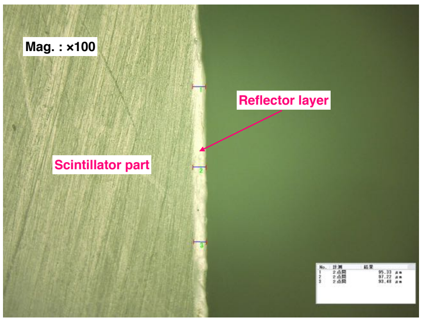

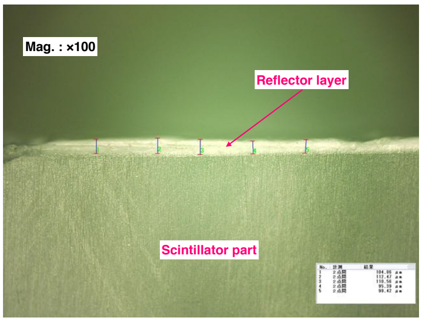

Figure 2.3: Microscopic observation of extruded cube cross sections

2.2.2 Wavelength shifting fiber

Wavelength shifting (WLS) fiber in Super-FGD is the same type as the current ND280. Its material is called Y-11(200) produced by Kuraray[12]. The main specifications are shown in Table 2.1. Absorption wavelength at 430 nm is matched with that of light emitted from the scintillator cubes.

	Specification
Fiber type	Round / Multi cladding
Dameter	1.0 mm
Materials	Core : polystyrene (PS) Inner clad : polymethylmethacrylate (PMMA) Outer clad : Fluorinated polymer (FP)
Refractive index	Core : 1.59 Inner clad : 1.49 Outer clad : 1.42
Density	Core : 1.05 g/cm^3 Inner clad : 1.19 g/cm^3 Outer clad : 1.43 g/cm^3
Peak emission wavelength	476 nm (green)
Peak absorption wavelength	430 nm
Attenuation length	$>$ 3.5 m

Table 2.1: Main specifications of the WLS fiber, Y-11(200)

2.2.3 Multi-pixel photon counter (MPPC)

The T2K experiment has been using the multi-pixel photon counters (MPPCs) produced by Hamamatsu Photonics in the current near detector since 2009[13]. The ND upgrade also adopted this photosensor. The MPPC type for Super-FGD is S13360-1325PE. $1.3 \times 1.3\text{mm}^2$ photosensitive area matches with the 1.0 mm diameter of the WLS fiber. This type is the surface mount package to minimize the installation space. The detailed specifications are summarized in chapter 3. The production of MPPCs will be finished by the end of 2019 and sequentially checked their characterization with similar method to the current near detector[14].

2.2.4 Readout electronics

The electronics for Super-FGD is planned to be developed based on an existing system for the other experiment due to the limited period of time. The base design is the Cherenkov Imaging Telescope integrated Read Out Chip (CITIROC) used in the Baby MIND detector deployed for the WAGASCI experiment[15]. CITIROC is frontend ASIC developed by Omega laboratory[16] and designed for the readout of a large number of MPPCs. It has two preamps with different gain, slow shapers, a fast shaper with a discriminator and an external digitizer. The frontend board with CITIROCs is under development.

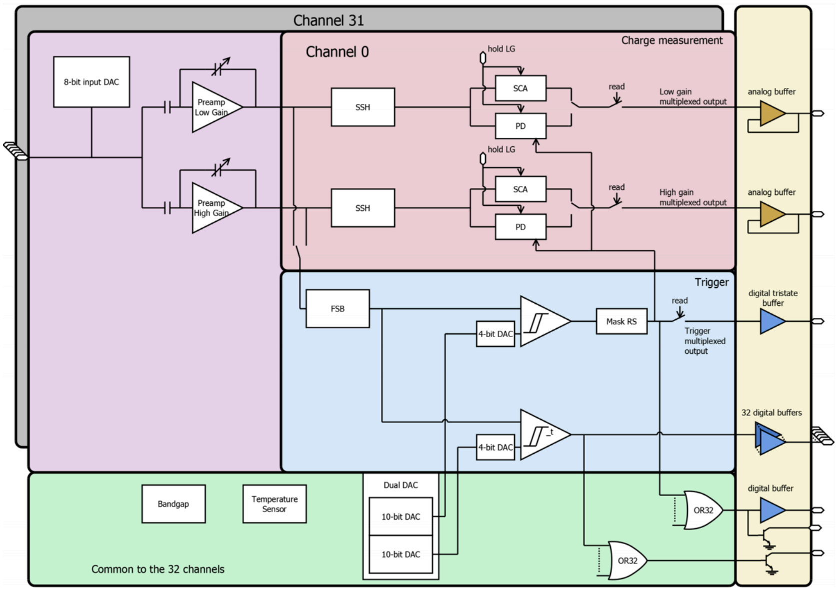

Figure 2.4: Block diagram of CITIROC

2.2.5 Optical interface

The optical interface connects MPPCs on the PCB with the WLS fibers and brings optical signals outside the detector. It has also the role of the interface to the frontend board connected via high density cables. The cross-sectional view of the optical interface is shown in Fig.2.5. The interface is located on the surface of the box panel made by AIREX foam and the carbon fiber skin. It is designed for MPPCs on an MPPC-PCB of 8×8 pitches. The scintillation light from the cubes is brought to the outside of the box via the WLS fibers which are fixed into the cylindrical holes in the plastic layer with the optical connectors. The MPPCs on the MPPC-PCB are coupled to the fibers inside the plastic layer holes. The holes provide optical separation between the MPPCs. The thickness of the plastic layer is 9 mm.

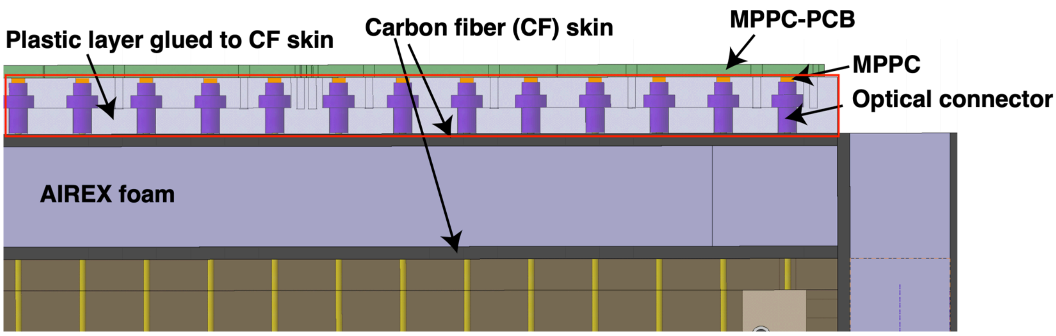

Figure 2.5: Cross-sectional view of the optical interface. The interface is the part in the red frame except for MPPCs.

Its performance was tested with 25 extruded scintillator cubes. It consists of a plastic plate, WLS fibers, fiber connectors and the PCB with 25ch surface-mount MPPCs. The plastic plate and fiber connectors are made by a 3D printer at CERN. The WLS fibers were glued to the connectors by the epoxy optical cement named EJ-500 which was also used for the current ND280 detectors. About 70 photo electrons (p.e.) per MIP was observed in average with <10% of RMS. Optical crosstalk between separated holes was also checked injecting LED light to a WLS fiber. No crosstalk was observed in 1 MIP level of light yield. These tests were performed with cosmic-ray, while we cross-checked its performance with the positron beam as shown in chapter 3.

(a) A plastic plate and fiber connectors

(b) WLS fibers and connectors

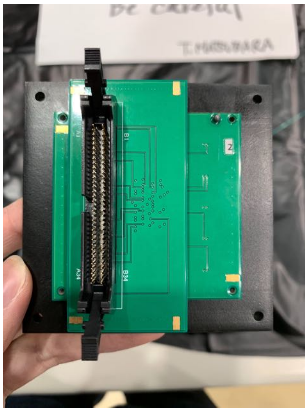

(c) The interface with a MPPC-PCB

Figure 2.6: The optical interface prototype

2.2.6 Cube assembly

Depending on the variation of the cube size, two problems are considered to be occurred. First one is the difficulty of the WLS fiber insertion into a cube array. If adjacent fiber holes are shifted more than 0.2 mm, the fiber insertion can be jammed by the gap between two cubes. Second one is the inaccurate positioning of WLS fibers to MPPCs. A fluctuation of a cube size leads to large deflection of fiber positions when the 2 million cubes are assembled. The cube produced by injection molding has a precise size variation of about 23 μm, which was measured in Russia. On the other hand, the assembling method for all the detector components is needed to be developed.

One of the assembly methods is called a "fishing line" method, which assembles the cube arrays with plastic threads. A fishing line of 1.3 mm diameter was used for the purpose. At first, the cube array is assembled with the fishing lines. The fishing lines are replaced by the WLS fibers one-by-one. This method was demonstrated with 9216 cubes in Russia as shown in Fig.2.7 and no problem was found with this assembly.

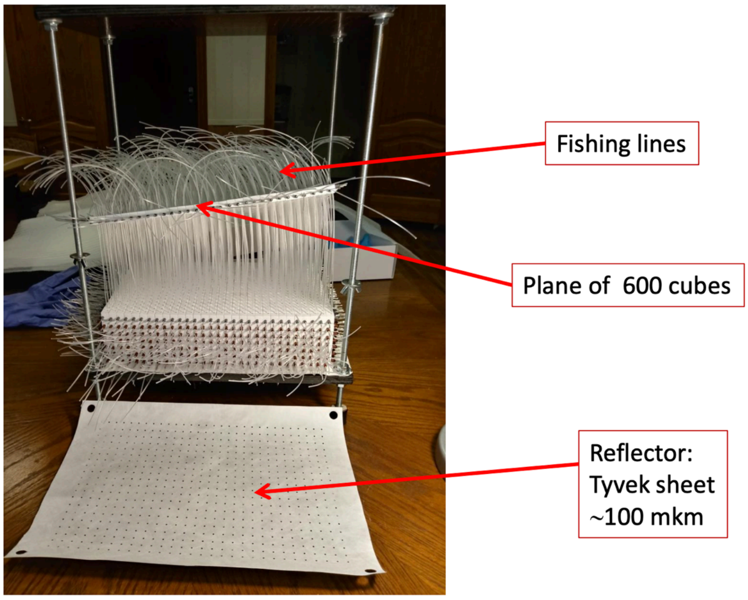

Figure 2.7: Assembling process of the scintillator cubes with the fishing lines

Another assembly method which uses a technique with ultrasonic welding is under development. The main idea is to assemble the plane modules which consist of cube arrays fixed on white thin sheets with controlled intervals. Each plane module is aligned and laminated in a container box for the full detector. The intervals between the cubes can absorb the variation of the cube size. Moreover, the assembly work is divided into smaller pieces thanks to the modular structure.

For this assembly of a plane module, ultrasonic welding method is under development. A white polystyrene sheet with a few hundred μm thickness is welded onto the cubes as following:

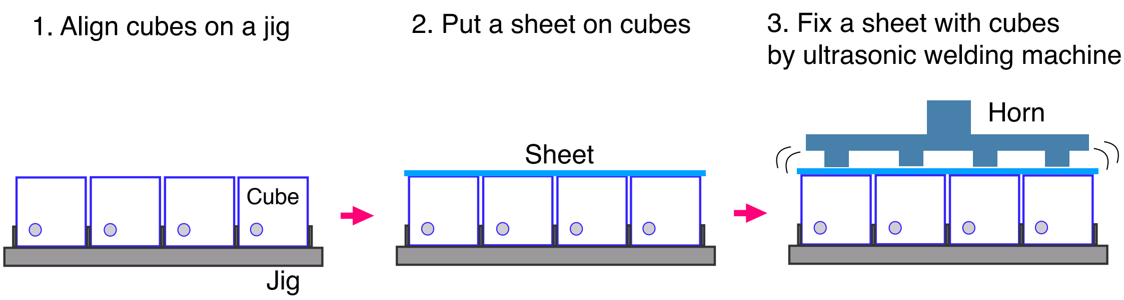

Figure 2.8: Assembly procedure of a plane module

1. Cubes are aligned on the dedicated jig which has thin grid plates to align the cubes precisely with intervals.
2. A white polystyrene sheet with holes is put on the cubes so that holes in the sheet are matched to ones in the cubes.
3. The white sheet is welded onto the cubes by an ultrasonic welding machine. Welded parts are dotted on a surface of the cubes avoiding the area close to the holes and edges.

This method was preliminarily demonstrated by some extruded scintillator cubes and white polystyrene sheets as shown in Fig.2.9. One of the concerns about this method is leakage of scintillation lights from the welding points. The light yield and optical crosstalk were checked with the positron beam and the results are shown in chapter 3.

Figure 2.9: Pictures of a welded cube. A polystyrene sheet was welded at several points in every about 1 mm avoiding the hole and the position close to edges.

2.3 Current status and tasks of Super-FGD R&D

As described in the previous section, R&D for the Super-FGD components is ongoing in preparation for the construction and installation. The scintillator cube, the WLS fiber and the MPPC have already designated each final type for the real Super-FGD. The first prototype of the optical interface was checked its performance with injected cubes. The electronics based on the CITIROC module is under development and the production of the first prototype FEB is foreseen for the forth quarter of 2019. On the other hand, several tasks need to be completed in terms of performance check.

For the real detector injection molding is planed to be used as a production method of scintillator cubes. Performance of the injected cubes should be surveyed in detail because this method itself is under development. It is important to validate the performance by comparing them to the extruded cubes which has been produced at the initial stage of R&D. Moreover, a check for non-uniformity of response in single cube is desired. The information of non-uniformity can be useful for charged particle tracking in neutrino interactions.

The ultrasonic welding method, which is a candidate of the assembly methods for Super-FGD, is expected to have the good workability and the scalability due to its modular structure. however, influence to performance of the cubes should be confirmed because this method melts a surface of a cube and a polystyrene sheet together in order to joint with each other. One of the concerns about the method is a leakage of scintillation lights from the welding points.

Some items remain to be ascertained in preparation for the final Super-FGD as shown above. In the beam test as described in next chapter, we checked the performance of the scintillator cubes, the welding method and the optical interfaces with several setups.

Chapter 3

Performance evaluation of Super-FGD prototype with a positron beam

3.1 Purpose of the beam test

The main purposes of the beam test are following:

1. Measurement of position dependence in single scintillator cube
2. Validation of the welding method in terms of observed light yield and optical crosstalk
3. Comparison of the response between extruded cubes and injected cubes
4. Confirmation of the performance of the optical interface

To achieve these purposes, measurements were performed with several configurations; (i) Single scintillator cube was placed on the beamline to check non-uniformity of response in a cube. (ii) To check light yield with welded cubes, single extruded cube with a welded polystyrene sheet was used. In addition, two extruded cubes was prepared to measure optical crosstalk with welded sheets. (iii) Both extruded and injected cubes were measured to compare performance. The 9(3×3)-cube setup was also prepared for comparison of optical crosstalk. (iv) Variation of light yield with the optical interfaces was measured with a 5×5×5 prototype. Tracking performance of the prototype was also checked.
Detailed explanation for the detector configurations is described in section 3.2.2.

In order to measure the position dependence of response, two hodoscopes were used to determinate particle tracks. One hodoscope consists of two thin layers overlapped perpendicularly with each other. Each layer consists of sixteen scintillating fibers. Detailed information for the hodoscopes are described in section 3.2.3.

3.2 Experimental setup

3.2.1 Beamline

The beam test was performed at the research center for Electron PHoton science (ELPH), Tohoku University. The positron beam is produced by two accelerators, a LINAC and a booster storage ring (BST ring). The electron beam produced in LINAC is accelerated with BST ring up to 0.8-1.3 GeV. The beam impinges on a graphite radiator and produces secondary gamma-ray which enters to the GeV γ irradiation room as shown in Fig 3.1. The gamma-ray beam impinges on a tungsten target to be converted into electron-positron pairs. The produced positrons are bent by 30° and separated from electrons by a dipole electromagnet. Parameters of the positron beam in this test are shown in table 3.1. In total 36 hours of beam time was assigned to our beam test.

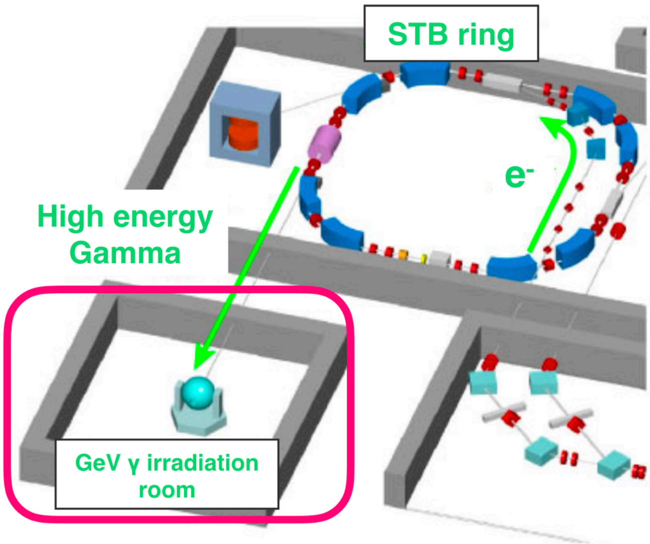

Figure 3.1: The GeV γ beamline[18]

Momentum	~ 500 MeV
Rate	~ 2.7 kHz
Spread	$\sigma_x = \sigma_y \sim 7$ mm
Duty cycle	35.7 % or 62.5 %

Table 3.1: Positron beam parameters

3.2.2 Detector setups

The schematic and pictures of the measurement system are shown in Fig. 3.2 and Fig. 3.3. The measurement system except for NIM modules was placed inside a $40 \times 40 \times 40$ cm^3 aluminum frame covered with black sheets. The center of beamline was located at a height of 161cm from the floor. Each detector and two hodoscopes were aligned along the beamline using laser marking devices and threads (300-400 μm diameter) stretched between hodoscopes. The optical interfaces were attached to the frame so that bending loss of scintillation lights in the WLS fibers was kept minimal. Optical signals were converted to electrical signals by MPPCs and transmitted to NIM modules via 1 m flat cables.

In all results, the three orthogonal directions are defined as following; (i) Z direction is the beam direction. (ii) Y direction is vertically upward. (iii) X direction configures a left-handed coordinate with the other two axes.

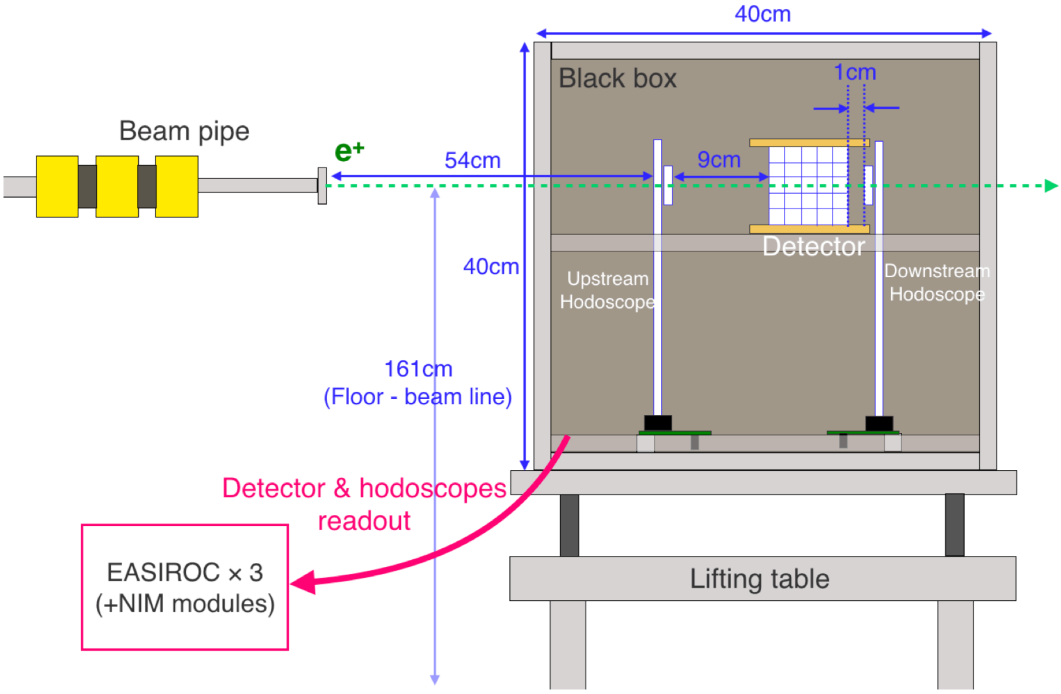

Figure 3.2: Schematic of the measurement system

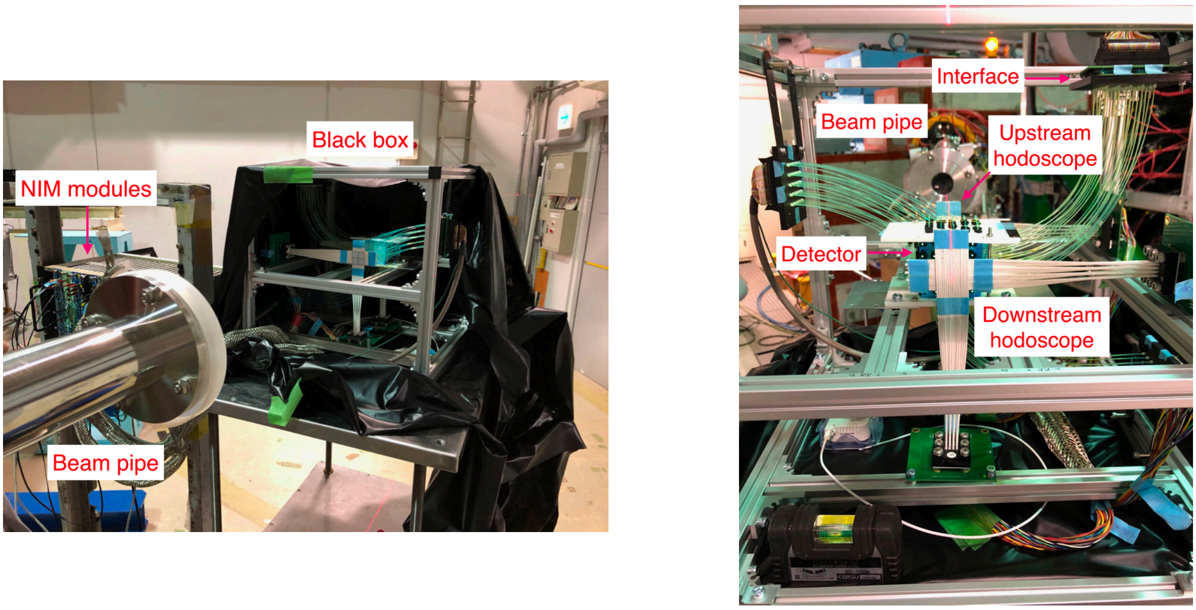

Figure 3.3: Pictures of the measurement system

Depending on the purpose of the measurement, the data were taken with four types of detector setup. Each configuration and purpose is shown in Table 3.2 and their pictures in Fig.3.4.

The 5×5×5-cube prototype consists of 125 injected cubes. In order to fix all cubes without an adhesive, they were covered by plastic wraps on the whole. This prototype was sandwiched by two plastic plates up and down to be fixed on the two aluminum frames in the black box. On the left and right sides of the bottom plastic plate were two aluminum plates with holes. The prototype could be moved or rotated by sliding these frames. When the prototype was rotated, it was fixed using the holes of aluminum plates as shown in Fig.3.5. The prototype was located so that its center was on the beamline even with the rotated configuration.

In the 1-cube configuration, an extruded cube and an injected one were measured respectively for a comparison of light yield. On the other hand, only an injected cube was used for the measurement of position dependence of optical response. The dedicated pedestal consisting of 4 acrylic cubes and a polystyrene plate with 1 cm wide was used in order to match their positions to the center of the beamline.

In the measurement for the performance of the welding method, 100 μm and 200 μm thick white polystyrene sheets were used separately. The sheet was welded onto one plane of an extruded cube. The positions of welded sheets had two patterns; (i) The sheet was behind the cube to the beam direction. (ii) The sheet was on the left side of the cube to the beam direction.

The 2-cube configuration used only extruded cubes. One cube was located on the beamline and the other on the left side of the fired cube to the beam direction. Two cubes were also on the same pedestal as the 1-cube measurement. The cubes with welded sheets were also used in this configuration as the ones where the events selected by the hodoscopes passed. The sheets were between two cubes in order to measure optical crosstalk with that.

The 9-cube configuration had a 3×3 arrangement and they were fixed by a frame made by 16 acrylic cubes. The acrylic cube has the same shape as the scintillator cube including the position of fiber holes. This setup was located so that the central scintillator cube was on the beamline. Optical crosstalk was compared between extruded cubes and injected ones in this configuration.

Setup	# of readout ch (X, Y, Z)	Cube type	Purpose
5×5×5-cube prototype	(25, 25, 25)	·Injection	·Ascertainment of light yield fluctuation for readout channels ·Validation of tracking (+15 & -15 mm shift) (15° & 30° rotation)
1 cube	(1, 1, 1)	·Injection ·Extrusion ·Extrusion w/ welding	·Position dependence of optical response ·Injection vs. extrusion with light yield ·Nominal vs. welding with light yield
2 cubes	(1, 2, 2)	·Extrusion ·Extrusion w/ welding	·Nominal vs. welding with crosstalk
9 cubes	(3, 3, 9)	·Injection ·Extrusion	·Injection vs. extrusion with crosstalk

Table 3.2: Configuration and purpose of each setup

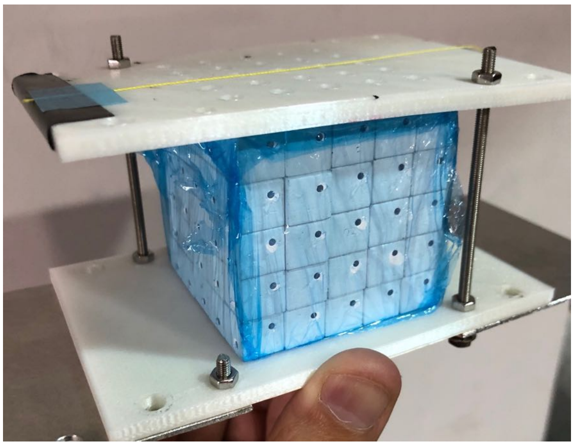

(a) 5×5×5 Super-FGD prototype

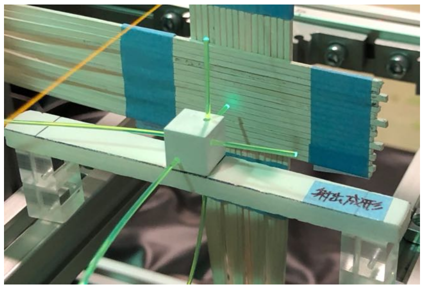

(b) 1 cube

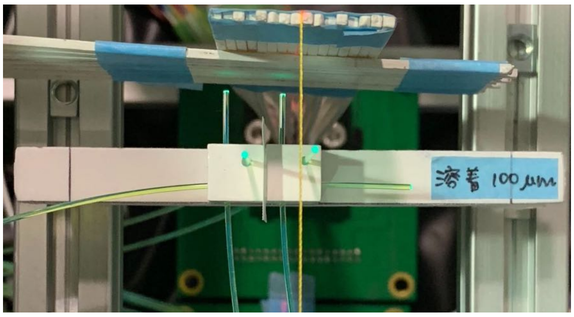

(c) 2 cubes

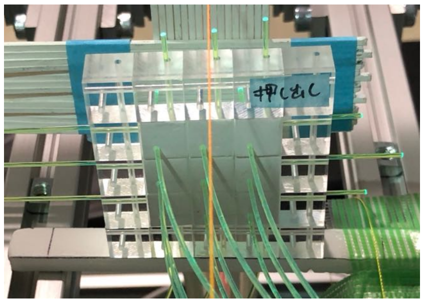

(d) 9 cubes

Figure 3.4: Setup of each detector

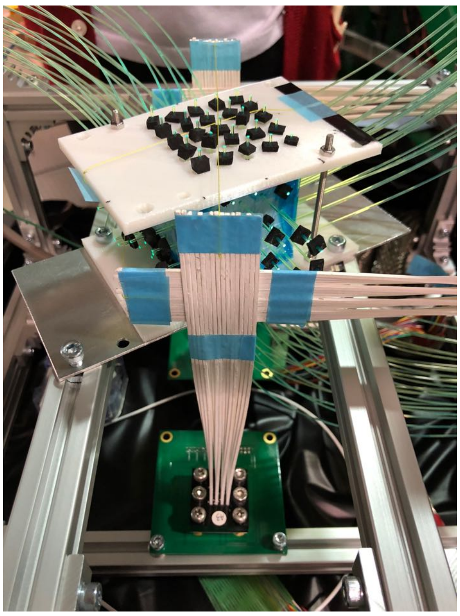

Figure 3.5: The 5×5×5-cube prototype with 30° rotation. The position of two aluminum frames for each configuration had been measured in advance.

Each WLS fiber Kuraray Y-11 was glued with a fiber connector by optical cement EJ-500. One end of the fiber was polished with a diamond polisher named FiberFin[19]. For the 5×5×5-cube prototype measurement, the average of fiber length in X,Y and Z readout direction was 29.3 cm, 31.2 cm and 27.5 cm, respectively. The difference of fiber length in the same optical interface was at most 5 cm and the light yield difference calculated by its attenuation length was about 1%. The bending diameter of was more than 30 cm in all fibers and loss of scintillation lights from the cubes was estimated at less than 1%. The readout fibers in other setups were selected from the central part of each interface to reduce bending tension to the fiber.

3.2.3 Hodoscopes

Fig.3.6 shows the front view of the upstream hodoscope. One hodoscope layer consists of sixteen polystyrene scintillating fibers aligned in a straight line. The size of each scintillating fiber is 20 cm in length and 1.5×1.5 mm^2 in cross section. About 100 μm thick white reflector was painted on the surface of each fiber. The area where two layers overlapped perpendicularly was 26×26 mm^2 in square measure. One end of each layer has a 4×4 arrangement of scintillating fibers and an arrayed MPPC was attached to that. The two hodoscopes have 64 readout channels in total. The 5×5×5-cube prototype was located so that the distance from the upstream hodoscope was 9 cm and from the downstream hodoscope was 1 cm, while the distances with the other setups were 10.5 cm and 1.5 cm respectively.

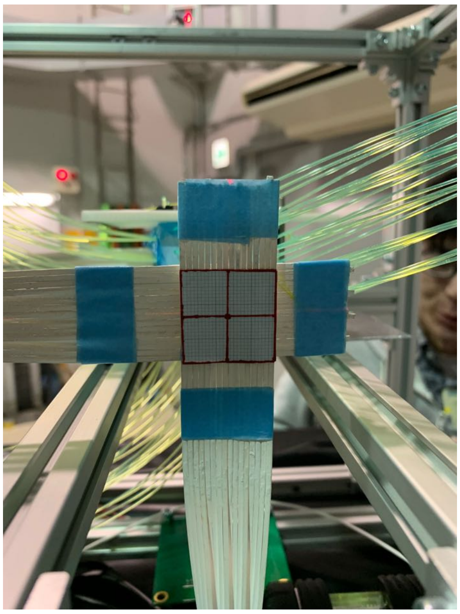

Figure 3.6: The upstream hodoscope

3.2.4 Multi-Pixel Photon Counter (MPPC)

Two types of MPPC were used as photon-counting devices. Structures and parameters of each MPPC are shown in table 3.3. In our beam test, S13360-1325PE was used for scintillator cubes and S13361-3050AE-04 for hodoscopes. Overvoltage for the former was about 4.5 V and for the latter about 2.5 V.

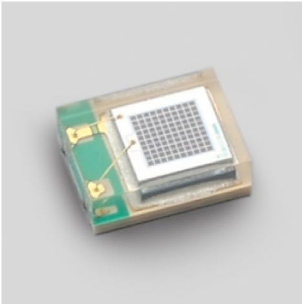

(a) S13360-1325PE

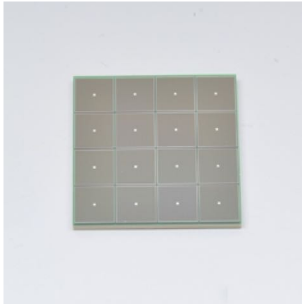

(b) S13361-3050AE-04

Figure 3.7: MPPC[11]

Item	Value of S13360-1325PE	 S13361-3050AE-04
Package type	Surface mount	with connector
Size of a pixel	25×25 μm	50×50 μm
# of pixels	2668	3584
Effective photosensitive area	1.3×1.3 mm	3×3 mm
Break down voltage (V_{bd})	53 ± 5 V	53 ± 5 V
Recommended operation voltage	V_{bd} + 5 V	V_{bd} + 3 V
Gain	7.0×10^5	1.7×10^6
Typical dark noise rate	70 kHz	500 kHz
Crosstalk rate	1 %	3 %
Photon detection efficiency	25 % (450 nm)	40 % (450 nm)

Table 3.3: Structures and paremeters of each MPPC

3.2.5 Readout electronics and data acquisition system

NIM EASIROC module[20] shown in Fig.3.8 was used for the main readout electronics. This module has two front-end ASIC named Extended Analogue SiPM Readout Chip (EASIROC) and each chip has 32 MPPC inputs. The bias voltage for MPPC is adjustable individually within the range of 0$\sim$4.5 V. Charge from MPPC was recorded with an ADC. In this test, the bias voltage to the MPPCs was adjusted in order to equalize a gain for each channel. The gain is defined as the difference of ADC counts between the peaks of pedestal and 1 p.e.(photo-electron) level.

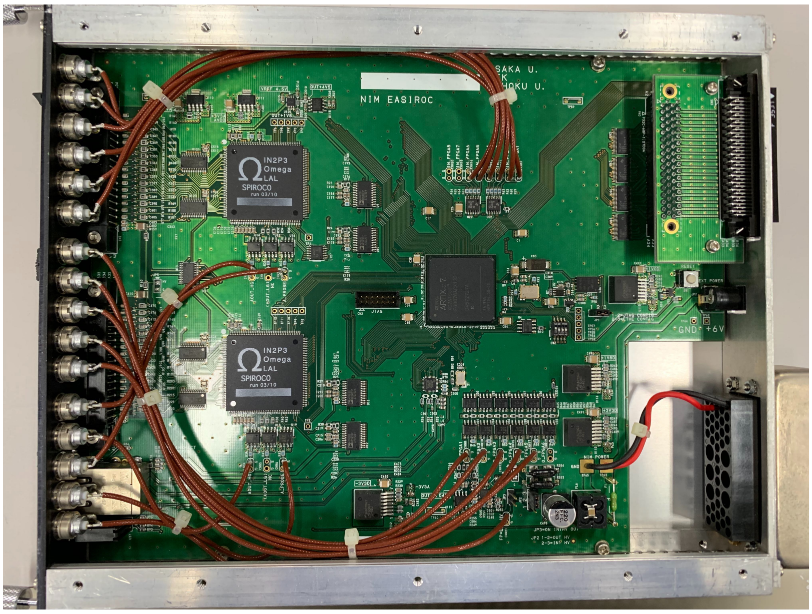

Figure 3.8: EASIROC module

The data acquisition system for our measurement is shown in Fig.3.9. Three EASIROC modules were used; one named UT_13 operated MPPCs for the two hodoscopes and the others named UT_11 and UT_12 operated MPPCs for the scintillator cubes. The SYNC OUT signal from UT_13 started taking the data by taking coincident signals with trigger signals. HOLD, T STOP and ACCEPT signals inputted in order to synchronize data acquisition of each EASIROC. The digital data was transmitted to the DAQ PC via Ethernet cables. However, sometimes mis-synchronization of EASIROCs was occurred accidentally in the measurement runs. The cause of mis-synchronization was not understood. However, at last about 70% of the entire measurement runs was used in the analyses and sufficient statistics was accumulated in all measurement setups.

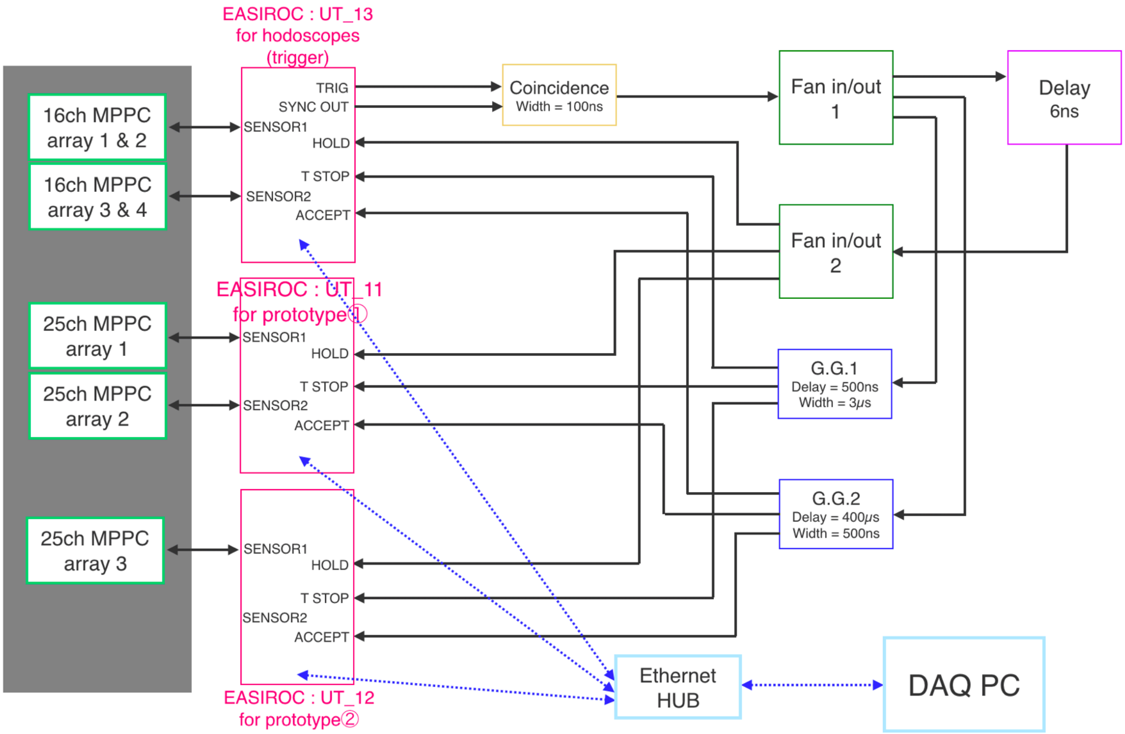

Figure 3.9: The diagram of digital signals

3.3 Data taking and gain calibration

3.3.1 Trigger configuration

The trigger configuration of the measurement required hits with more than 2.5 p.e. in all four hodoscope layers. The threshold for the hodoscopes was sufficiently lower than light yield of more than 10 p.e. in each scintillating fiber. Moreover, noise level of less than 2.0 p.e. like the dark noise and the after pulse in MPPCs was cut by this threshold. However, because the size of the $5\times5\times5$-cube prototype was larger than the area covered with the two hodoscopes, the beam data was taken for the gain calibration of the $5\times5\times5$-cube prototype with the trigger by only the upstream hodoscope before and after the measurement runs. It was also confirmed that the gain was not changed during the measurement.

3.3.2 Gain calibration

Examples of typical charge distribution with the beam data are shown in Fig.3.10. The most left peak corresponds to the pedestal events and the right one next to the pedestal corresponds to the 1 p.e. level events in each distribution. The peak ADC counts of pedestal and 1 p.e. level are identified as means of each fitted Gaussian function. A fitting range was determined in each EASIROC chip because one chip had 32 channels and corresponded to the upstream hodoscope, the downstream hodoscope, the detector readout of X, Y and Z direction. Even though the fitting ranges in the charge distributions was different between the readout channels, it was confirmed that the mean value of each fitted function corresponded to the ADC counts of the peak by sight. A coefficient to convert ADC counts to photo-electrons was calculated the difference between these two means:

$$\text{The conversion coefficient} = \tag{3.1}$$
$$(\text{ADC counts of the 1 p.e. level}) - (\text{ADC counts of the pedestal}).$$

From this gain, light yield of an event in a readout channel was calculated as following:

$$\text{Light yield [p.e.]} = \tag{3.2}$$
$$((\text{ADC counts of the event}) - (\text{ADC counts of the pedestal}))/(\text{The conversion gain}).$$

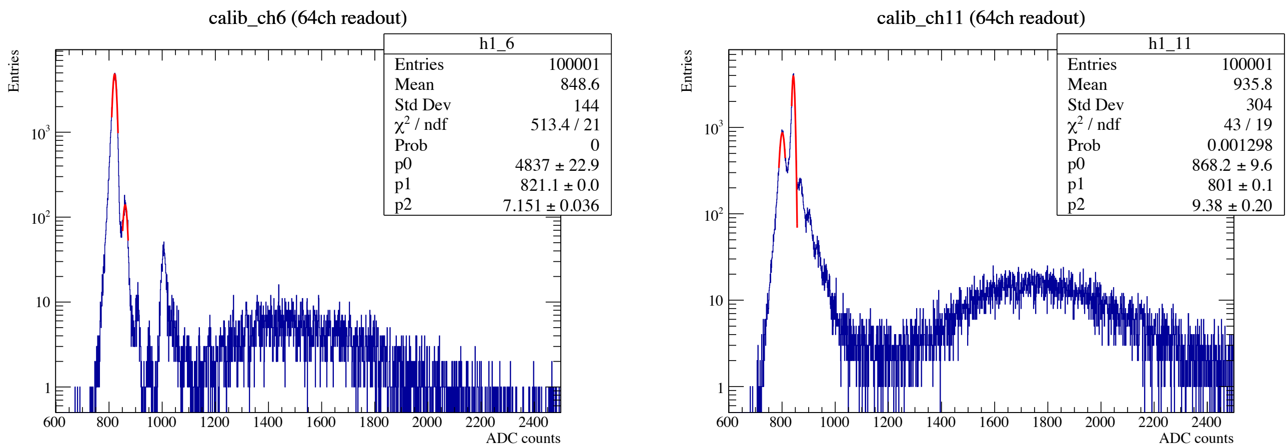

Figure 3.10: Examples of typical charge distribution with the beam data (left: MPPC for the hodoscopes, right: MPPC for the scintillator cubes). Each MIP-like event corresponds to the peak around 1500 and 1700 ADC counts.

Fig.3.11 shows the gain distribution of the run for the 5×5×5-cube prototype measurement. The ratio of RMS to a mean of the gain in each hodoscope or readout direction for the prototype was 3∼7%. The gain of other measurements (for 1 cube, 2 cubes and 9 cubes) was calibrated by the data of each measurement run itself. The gain for each measurement run also had variations of about 5% in each hodoscope and readout direction for the scintillator cube setup.

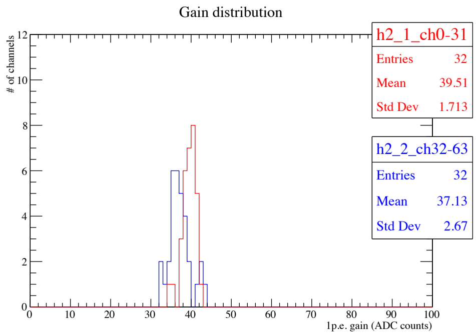

(a) Red: upstream hodoscope
Blue: downstream hodoscope

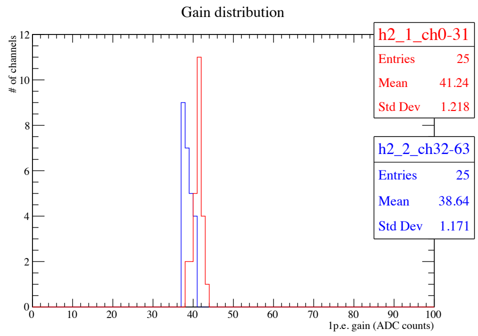

(b) Red: X readout
Blue: Y readout

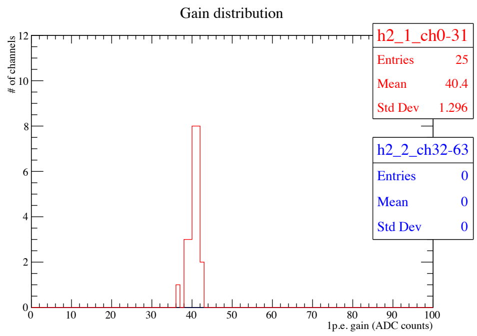

(c) Z readout

Figure 3.11: gain distribution of the run for the $5 \times 5 \times 5$-cube prototype measurement

3.3.3 Event selection and statistics

The position of the particle track was determined by the area named "cell" which two scintillating fiber overlapped with each other as shown in Fig. 3.12. The hit threshold for a cell is also more than 2.5 p.e. in both scintillating fibers. Figure 3.13 shows the hit count distribution in each hodoscope layer. The events with more than or equal to two hits in each hodoscope layer were less than 12% and excluded from analyses. In the results from section 3.4, the events called "good events" are defined as the ones which have hits in the given upstream cell and the downstream cell corresponding to the same position as the former. The good events in each cell were used in the analyses for the measurements of 1 cube and 9 cubes in order to measure the detailed response of the scintillator cube(s).

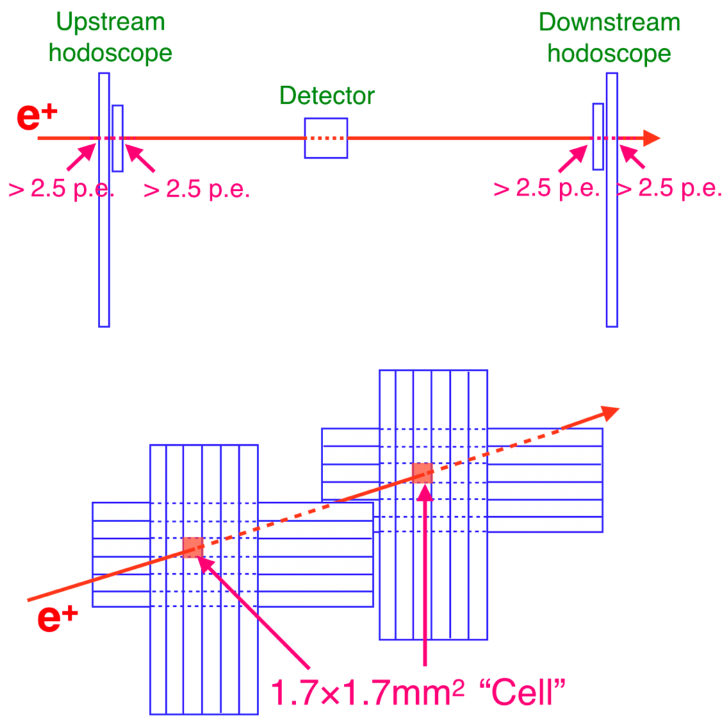

Figure 3.12: Particle tracking with two hodoscopes

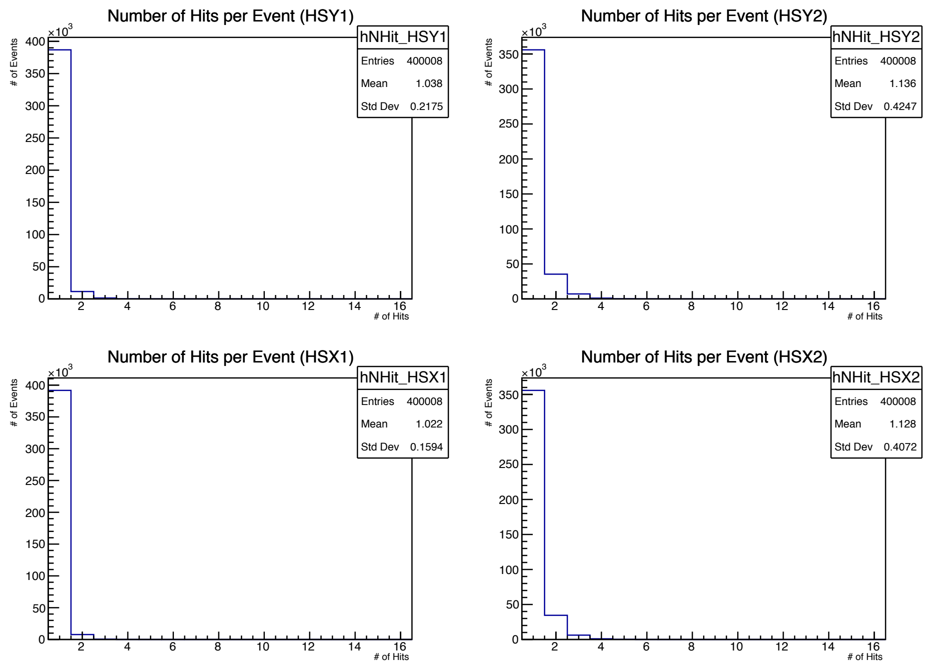

Figure 3.13: Hit multiplicity in each hodoscope

Each measurement run took 50,000 events and the run was repeated at least 10 times in each detector setup. In the cell where the good events passed through the scintillator cubes, at least 300 good events were required for the determinations of observed light yield (defined in section 3.3.2) with uncertainty of less than 5%. When mis-synchronization between the three EASIROCs happened accidentally in a measurement run, the run was not used in the analysis. In total, about 70% of the measurement runs was used.

Fig.3.14 shows an example of the hit counts for each hodoscope in a measurement run with 50,000 events. The left and central plots are the hit counts of each upstream and downstream cell respectively. The hit counts in these two plots were calculated independently. The right plot shows the number of the good events in each cell. The number of events for the cells of X=9 in the both hodoscopes is about 40-60% lower than that of the horizontally adjacent cells. The cause of this is considered to be a bad connection between the scintillating fiber and MPPC. In each measurement of the detector setup, the requirement of more than 300 events in each on-cube cell was satisfied even in the cells of X=9.

As of the beginning of the measurement, both hodoscopes were aligned with better than 300 μm of position accuracy for X and Y directions thanks to the threads and the laser marking devices. However, several measurement runs had the worse alignment than the first configuration due to touching the hodoscopes during changes for the setup. The measurement runs with mis-alignment were modified in the analysis by shifting the hodoscope cells vertically or horizontally. Figure 3.15 shows an example of hit counts when a given upstream cell is focused on. If the downstream cell with the largest number of hits is out of the same position corresponding to the focused upstream cell, all downstream cells are shifted so that the positions of these cells are matched with each other.

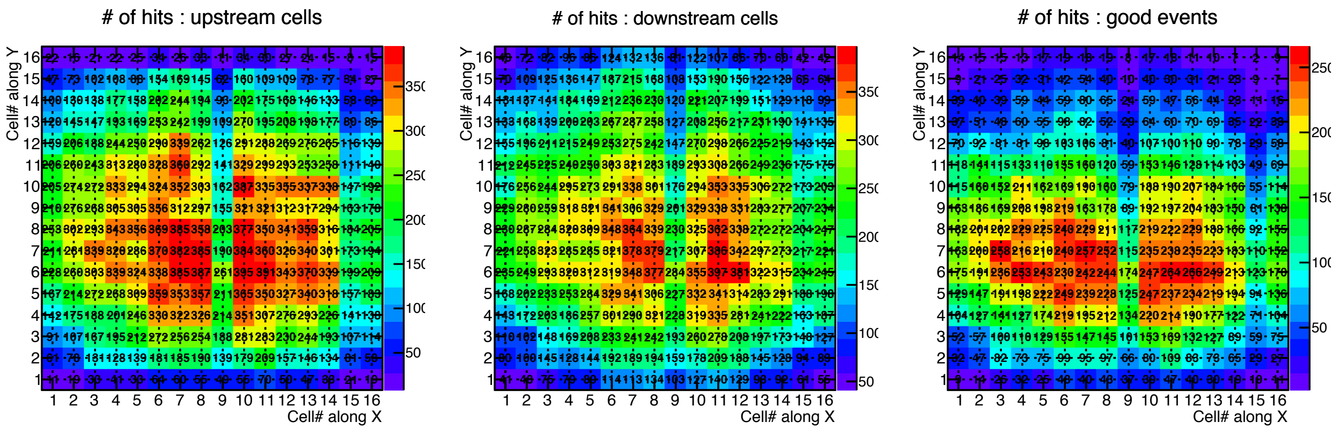

Figure 3.14: An example of hit counts for each cell in the hodoscopes

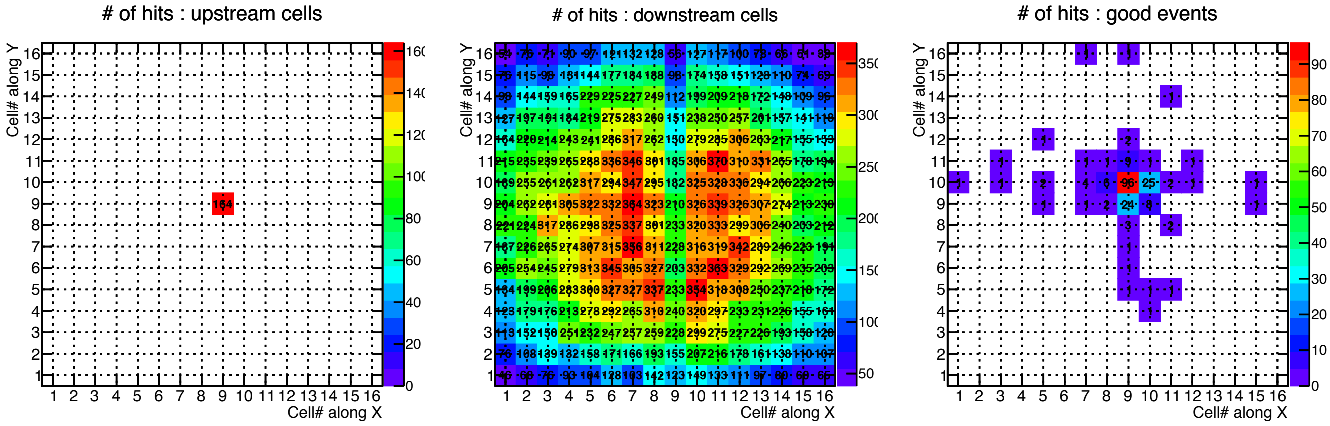

Figure 3.15: An example of hit counts when a given upstream cell (X=9, Y=9) is focused on. As shown in the right plot, the cell which has the largest hit counts is located in the adjacent cell (X=9, Y=10). The positions are corrected in the analysis so that they are matched with each other.

3.4 Results of the beam test

3.4.1 The response in single cube

In this section, the results of an injected cube measurement are shown. Figure.3.16 shows light yield distribution in each readout fiber. observed light yield was defined as the most probable value (MPV) of a fitted landau function in the distribution for each readout fiber. The fitting range was determined so that the value of χ^2/ndf in each distribution was less than 10. The central channel was selected from 5×5 readout fibers in each readout direction. Hit threshold in the prototype required the hit with more than 5.5 p.e. in all readout channels. This threshold was sufficiently lower than about 30 p.e. of expected light yield in a scintillator cube and higher than the MPPC noise level. Observed light yield in the X, Y and Z direction was 28.7 p.e., 25.4 p.e. and 29.6 p.e., respectively. This value is comparable to that of the current FGD[21] and sufficient as signals because zero value is out of 3σ section of a fitted landau function.

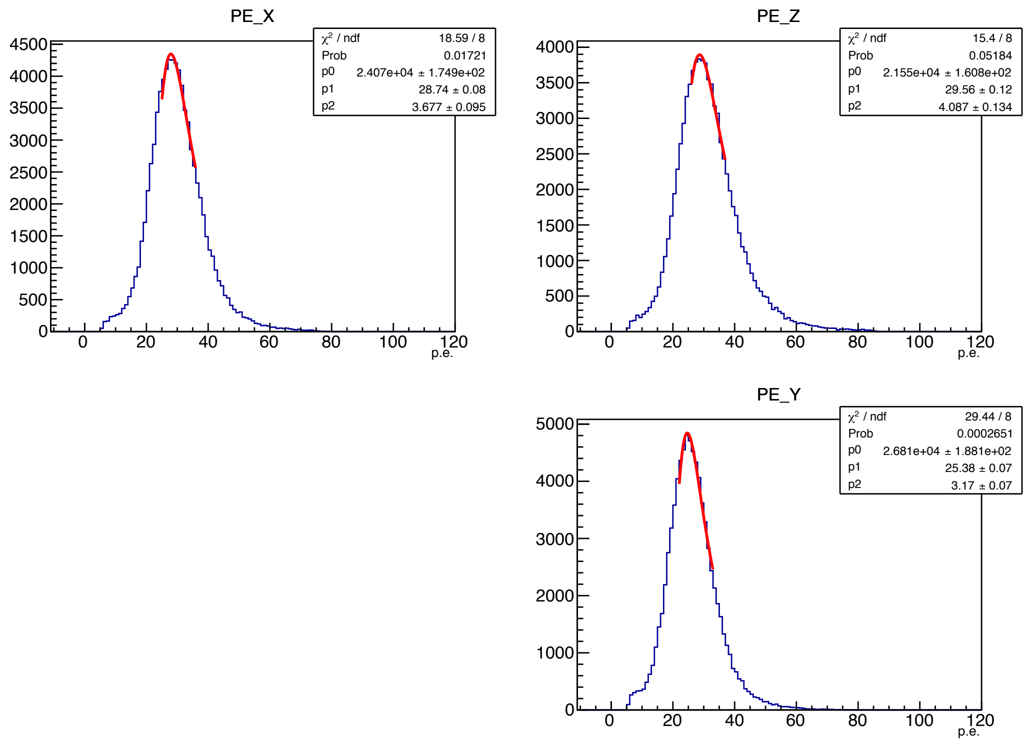

Figure 3.16: Light yield distribution for each readout fiber (an injected cube)

The position dependence of observed light yield in an injected cube is shown in Fig.3.17. The cell number along the X and Y direction corresponds to the number shown in Fig.3.14. The good events in each cell were used with the inner hodoscope area of 10×10 cells. The value at each cell covering the cube is defined as MPV of a fitted landau function, while that at each cell not covering the cube as mean of the light yield distribution. The left, central and right plot shows light yield from the X, Y and Z readout fiber in each cell position, respectively. All plots show the tendency that less light yield is observed at far cells from each corresponding readout fiber and along the other fibers.

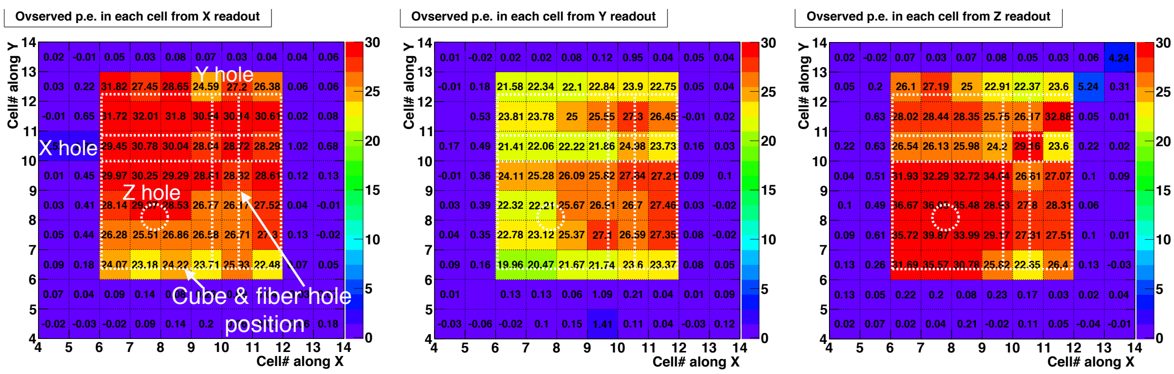

Figure 3.17: Position dependence of observed light yield in single injected cube. White dot lines show the position of the scintillator cube and each readout hole.

Another cause of non-uniformity of light yield in the cube is considered to be the acceptance of the readout fiber. For example, if a positron passes around the X readout fiber, scintillation lights have a tendency to be absorbed by the X fiber and not by the Y and Z fiber. Moreover, the Z fiber has a larger acceptance to scintillation lights compared with the X and Y fiber due to parallelity with the beam.

The position dependence of detection efficiency in an injected cube is shown in Fig.3.18. In this analysis, detection efficiency in each cell is defined as:

$$\text{Detection efficiency} = \frac{\#\text{ of good events with} > 5.5\text{ p.e. in each readout fiber}}{\#\text{ of all good events}}. \tag{3.3}$$

The position of the cube and the fiber holes in Fig. 3.17 and 3.18 was estimated by the values of detection efficiency on the cells which corresponded to the cube-edge position. For example, in Fig. 3.18, the cube position along the Y axis was estimated by a balance between the values on Y=6 and Y=12.

Almost all central on-cube cells have high detection efficiency of more than 99%. That of the area near the cube-edge is lower than the others according to the protruding area from the cube. Moreover, about 40% (10%) reduction of detection efficiency is observed in the Z fiber area for X and Y (Z) readout.

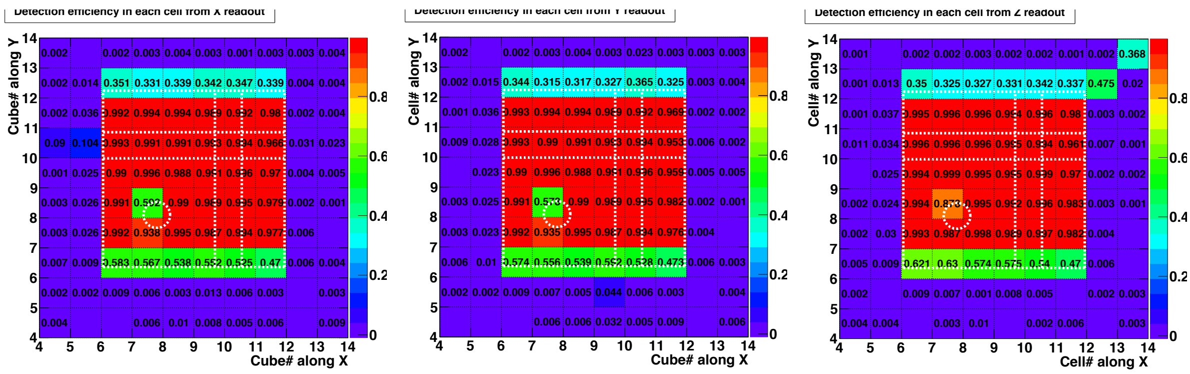

Figure 3.18: Position dependence of detection efficiency in an injected cube

Considering the actual situation, the effect caused by the parallel readout fiber to charged particles is considered to be much smaller than this beam test because few charged particles produced by neutrino-nucleus interactions go in parallel to the three orthogonal directions.

As shown the upper right part of the Z readout plots in Fig.3.17 and 3.18, larger values are observed compared with that of the other off-cube cells. Light emission from the external Z readout fiber is considered to be caused this increase. The Z readout fiber traversed the region where the good events were possible to pass due to the position of the optical interface as shown in Fig.3.19. Light yield from the WLS fiber is estimated about 5-10 p.e. with an angular dependence from the light yield distribution of the upper right off-cube cells. However, the detailed mechanism of light emission from the fiber with charged particles is not surveyed in this result.

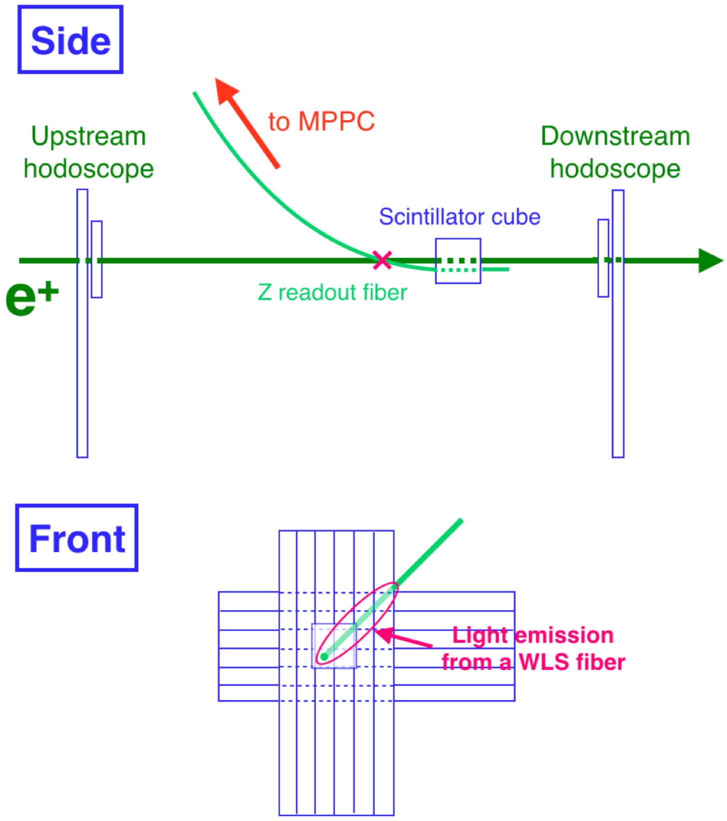

Figure 3.19: Light emission from WLS fibers

3.4.2 Measurement with welding sheets

The measurements with polystyrene sheets welded to an extruded cube were performed in order to check the influence of a technique with ultrasonic welding as an alternative assembly method. In particular, it was confirmed whether scintillation lights were leaked from the welding points or not. 100 μm and 200 μm thickness of polystyrene sheets were welded onto the surface of the extruded cubes respectively. The positions of welded sheets to the beamline are shown in Fig. 3.20. The cube was placed so that the sheet was parallel or perpendicular to the beamline.

Firstly, it was ascertained that reduction of light yield was observed or not for each readout fiber with a welded sheet in the single cube measurement. Evaluation method of observed light yield is the same as the previous section. Table 3.4 shows observed light yield with each configuration.

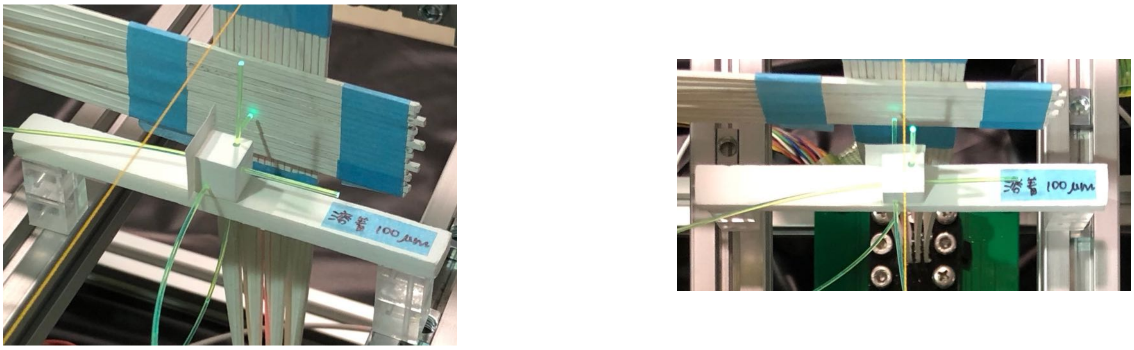

Figure 3.20: Position of a welding sheet to the beam line (left: horizontal, right: vertical)

Readout fiber	Configuration	Observed L.Y. [p.e.]
X	Non-welding	28.3
	w/ 100 μm sheet (Horizontal)	30.0
	w/ 200 μm sheet (Horizontal)	29.1
	w/ 100 μm sheet (Vertical)	29.4
	w/ 200 μm sheet (Vertical)	29.8
Y	Non-welding	24.3
	w/ 100 μm sheet (Horizontal)	26.8
	w/ 200 μm sheet (Horizontal)	25.5
	w/ 100 μm sheet (Vertical)	26.6
	w/ 200 μm sheet (Vertical)	25.9
Z	Non-welding	29.2
	w/ 100 μm sheet (Horizontal)	32.7
	w/ 200 μm sheet (Horizontal)	31.6
	w/ 100 μm sheet (Vertical)	30.7
	w/ 200 μm sheet (Vertical)	31.2

Table 3.4: Observed light yield in each readout fiber with several configurations

Table 3.4 shows not so much reduction of light yield with a welded sheet as about 5-10% increase from the non-welding configuration. It is considered that the effect of increasing reflection with a welded sheet is larger than that of leaking light from the welding points. On the other hand light yield difference of less than 5% was observed depending on the direction to the beam or thickness of welded polystyrene sheets. Even if the welding method is used for assembly of the real detector, no reduction of light yield would be confirmed so far.

Secondly, crosstalk rate was compared between the extruded cubes with and without a welded sheet in the 2-cube measurement. The fired cube with a welded sheet was located so that a sheet was in parallel to the beamline and between the two cubes. The events which satisfied the following requirements were used in this analysis:

- The events passed through inner 4×4 cells to assure that the positrons passed through the central part of the cube

- Observed light yield in the fired cube was more than 5.5 p.e.
- Ratio of L.Y. in the adjacent cube to that in the fired cube was less than 1 to remove the events scattered to the adjacent cube accidentally

Figure 3.21 shows the crosstalk distributions for two non-welding cubes. In this analysis, crosstalk rate for each readout direction was measured event-by-event and defined as mean of the distribution of the ratio of light yield in the adjacent cube to that in the fired one. In order to reduce false crosstalk due to pedestal fluctuations, light yield less than 0.5 p.e. in the adjacent cube was accepted as zero value. Table 3.5 shows crosstalk rate with each condition. The rates without a welded sheet are about 3% and these with a sheet are about 30% less than the former. It is considered that more scintillation lights are reflected thanks to the white polystyrene sheet between the two cubes. No deterioration of performance with welding method was confirmed in terms of optical crosstalk.

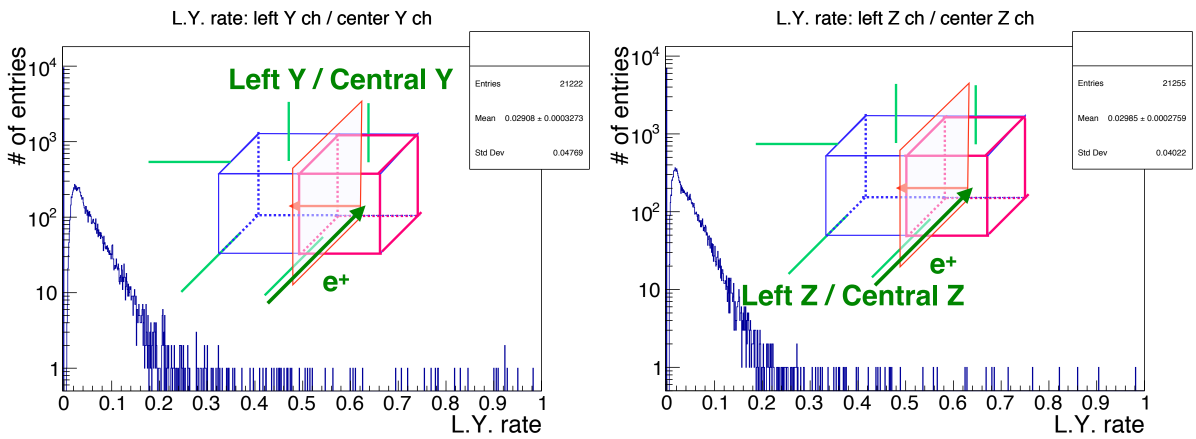

Figure 3.21: Crosstalk rate in non-welding cubes (left: Y readout, right: Z readout)

Readout fiber	Configuration	Crosstalk rate [%]
Y	Non-welding+Non-welding	2.91
	Non-welding+100 μm sheet	2.16
	Non-welding+200 μm sheet	2.49
Z	Non-welding+Non-welding	2.99
	Non-welding+100 μm sheet	2.06
	Non-welding+200 μm sheet	2.04

Table 3.5: Crosstalk rate with welding sheets. Extruded cubes were used in all configurations.

3.4.3 Comparison between extruded cubes and injected cubes

The measurements with the scintillator cubes made by injection molding were performed in order to compare their optical response with that of the extruded cubes. Observed light yield in each readout fiber for single cube is shown in Table 3.6. Observed light yield was evaluated in the same way as section 3.3.2. The difference of observed light yield between an extruded cube and injected one was less than 5%. No reduction of observed light yield was confirmed comparing an extruded cube to injected one.

Readout fiber	Production type	Observed L.Y. [p.e.]
X	Extrusion	28.3
	Injection	29.1
Y	Extrusion	24.3
	Injection	25.5
Z	Extrusion	29.2
	Injection	29.7

Table 3.6: Observed light yield for each readout fiber in single cube (extruded vs. injected cubes). The light yield distribution for the injected cube is shown in Fig.3.16.

In the 9-cube measurement, the crosstalk rate at surfaces and corners of a scintillator cube was compared between two types of the cubes. 9 cubes were aligned so that a 3×3 side faced on the beam pipe and the beam passed through the central cube. The scintillator cubes were surrounded and fixed by 16 acrylic cubes glued with each other (see Fig.3.4). The requirements to the events and the method to calculate crosstalk rate were the same as the previous section.

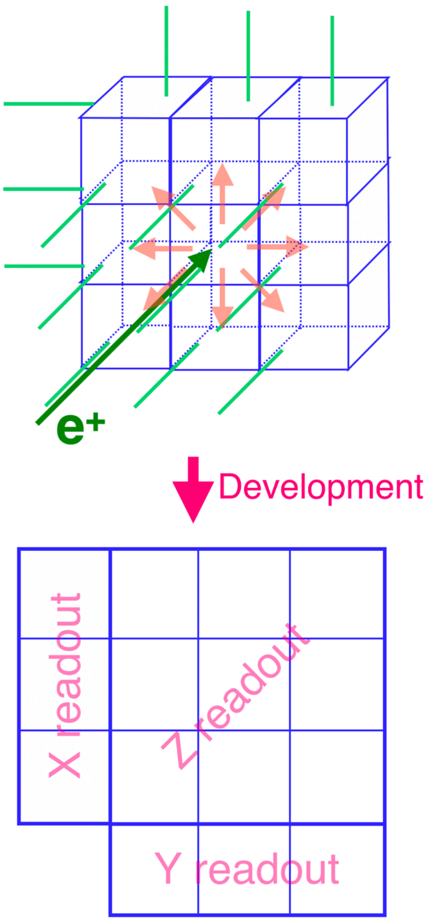

3.05	1.91	4.44	2.05
[X center]	4.48	[Z center]	3.95
4.41	(3.34)	4.34	1.45
CT rate [%]	3.80	[Y center]	3.37

(a) Extruded cubes

2.58	1.38	3.61	1.63
[X center]	3.48	[Z center]	3.53
4.28	(3.66)	3.75	1.30
CT rate [%]	2.86	[Y center]	2.82

(b) Injected cubes

Figure 3.22: Crosstalk rate in each position for 9cubes (extruded vs. injected cubes)

The right part of Fig. 3.22 shows the lists of crosstalk rate for the 9 cubes produced by each production method. Each cell corresponds to the channel position when the 9-cube array was developed to the plane figure as shown in the left part of Fig.3.22. The Z readout channel in the lower left cube was not used in the evaluation because this fiber traversed the selected region where the selected events passed and emitted extra lights like Fig.3.19. The average of crosstalk rate at surfaces for The Z readout fiber is 4.3% for the extruded cubes and 3.6% for the injected cubes. The average of crosstalk rate at corners for the Z readout is 1.8% and 1.4%, respectively. In total, about 20% reduction of crosstalk rate was observed from the extruded cubes to the injected cubes.

Compared with crosstalk rate measured with the extruded 2-cube configuration shown in the rows "Non-welding+Non-welding" on Table 3.5, crosstalk rate with the 9-cube configuration is about 30∼50% higher for the corresponding readout channels which are in the left cells to the Y or Z central ones in Fig. 3.22. It is considered that scintillator cubes have been compressed by surrounding acrylic cubes and their adjacent reflector layers have became thiner. In order to measure this effect quantitively, however, the pressure applied to the scintillator cubes is needed to be monitored.

The position dependence of detection efficiency for 9 cubes in each readout direction are shown in Fig.3.23. The good events passed through the inner 15×15 cells were selected in this result. Detection efficiency in each cell was defined as the ratio of the number of good events with more than 5.5 p.e. for any readout fibers in the same readout direction to the number of all good events. Other cut criteria was the same as the single cube result shown in the section 3.3.2. Reduction of efficiency in the Z fiber position was observed. Moreover, the efficiency in particular at the vertical boundary of the cubes was lower than that of the neighboring cells. This is caused by the gap between the cubes and thickness of the reflector layers. However, it is difficult to distinguish the two causes from this result because the pressure applied on the scintillator cubes was not evaluated in this measurement. On the other hand, reduction of the efficiency at the horizontal boundaries was unclear due to a tilt of the 9-cube array by pushing tension of the Z readout fibers as shown in Fig.3.24.

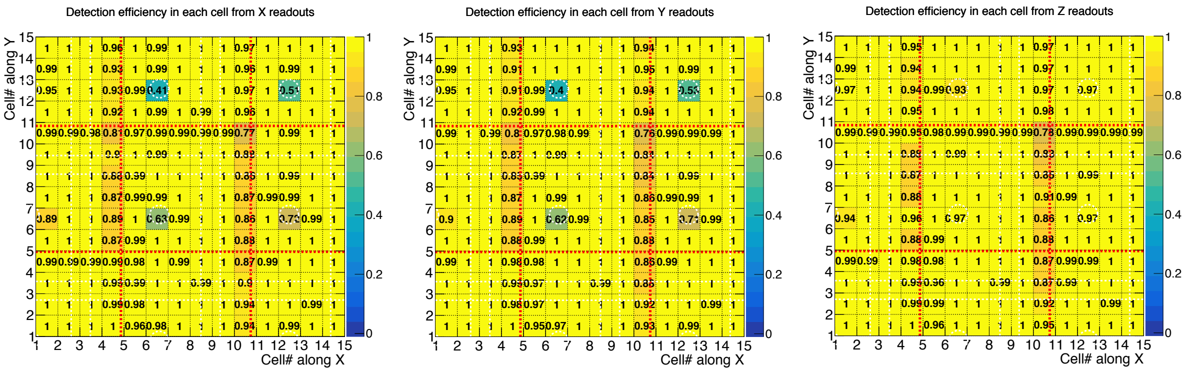

(a) Extruded cubes

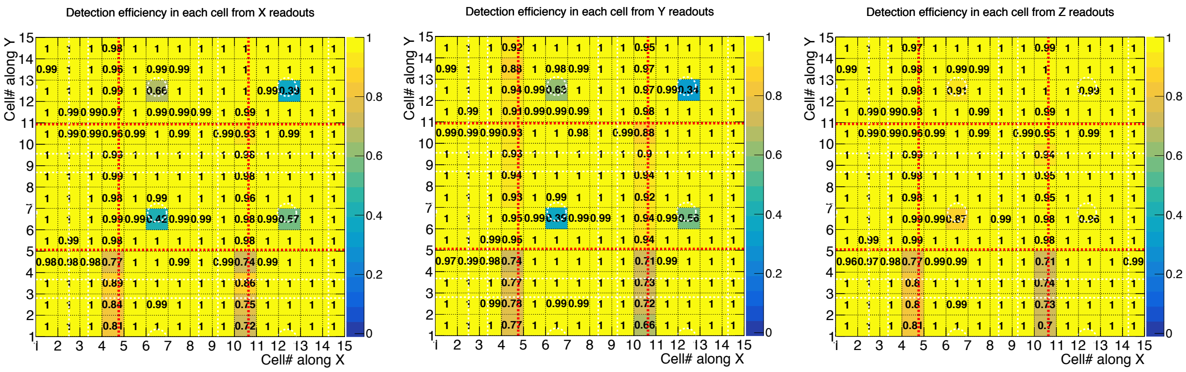

(b) Injected cubes

Figure 3.23: The spacial distribution of detection efficiency for each cube type and readout direction

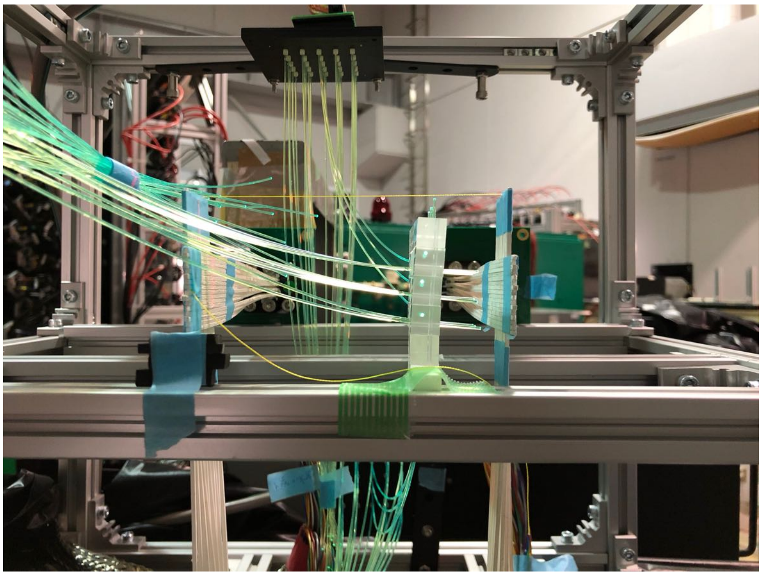

Figure 3.24: The side view of 9 cubes. The 9-cube array was pushed and tilted by the Z readout fibers.

3.4.4 Prototype with 125 (5×5×5) cubes

The 5×5×5-cube prototype was measured in different positions to the beam keeping X and Y position of the hodoscopes unchanged. Fig.3.25∼Fig.3.27 show the hit counts for all channels with ±15 mm parallel shift in X direction and 15°/30° rotation from the initial position. The left(right) figures are these of the upstream(downstream) hodoscope and the central three are these of the prototype for each readout direction. Examples of event display for each configuration are also shown in Fig.3.28. Synchronization between the three EASIROCs is confirmed with these event displays because the different EASIROC was used to record the ADC data of the hodoscopes, the X and Y readout channels of the 5×5×5-cube prototype and the Z readout channels, respectively. The effect of parallel shift or rotation can be seen in each plot.

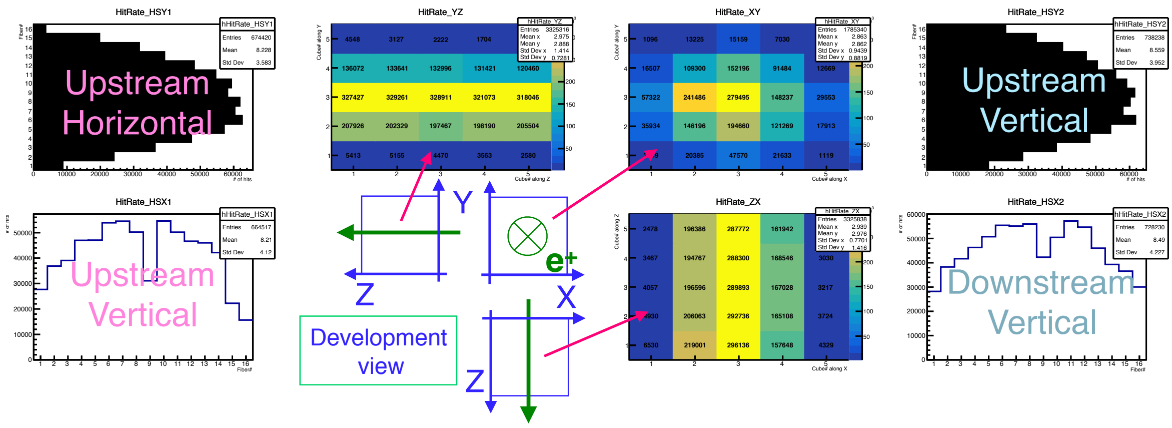

Figure 3.25: Hit rate for all channels with initial position. The relationship between the beamline and readout directions is shown in central part.

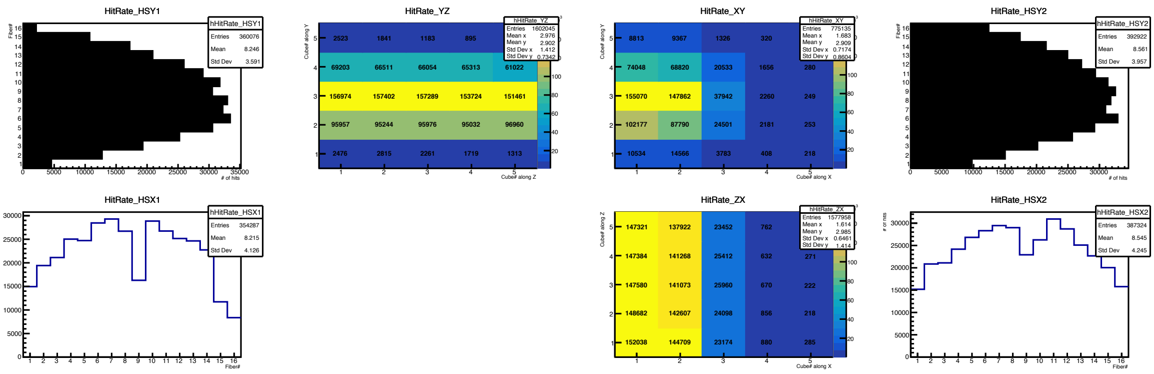

(a) +15mm parallel shift

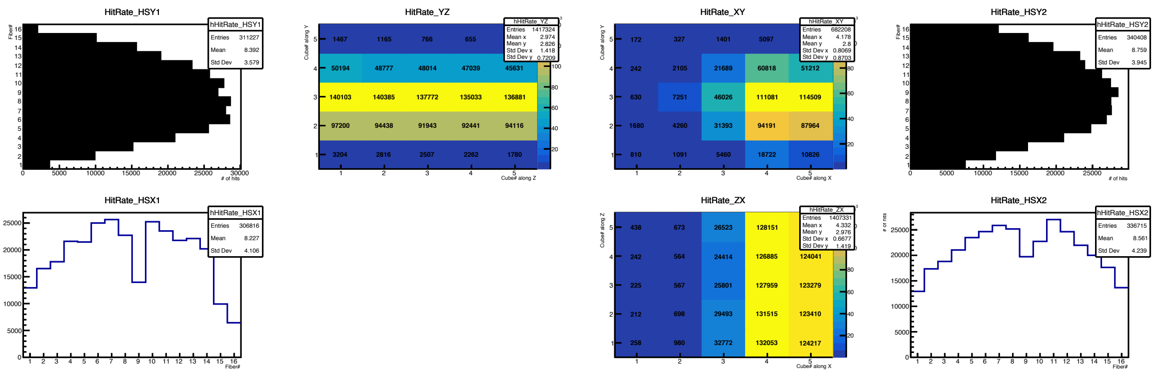

(b) -15mm parallel shift

Figure 3.26: Hit rate for all channels with parallel shift

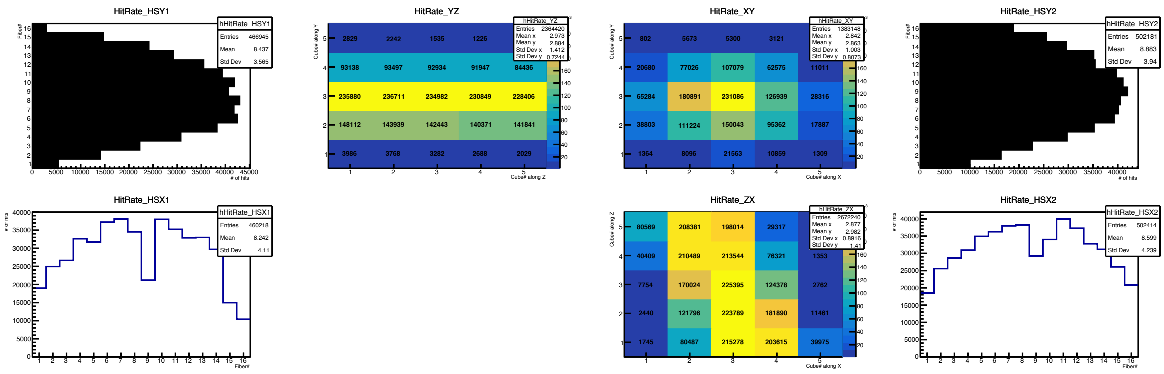

(a) 15° rotation

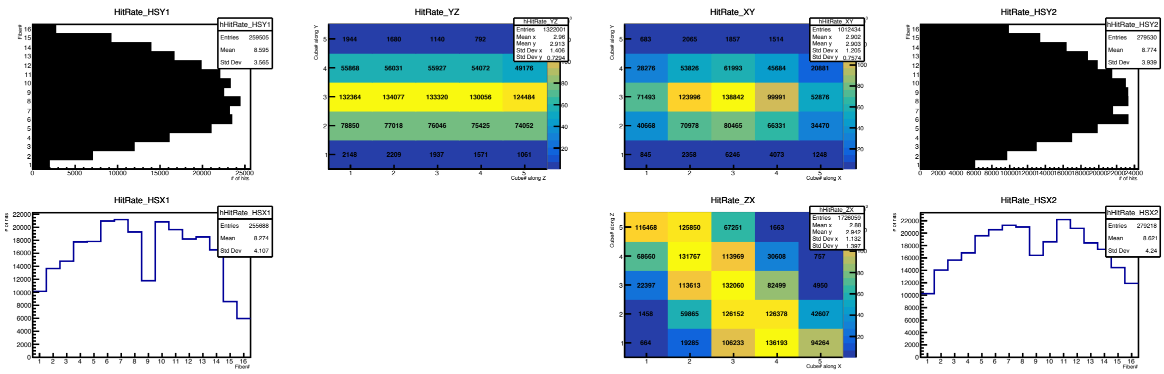

(b) 30° rotation

Figure 3.27: Hit rate for all channels with rotation

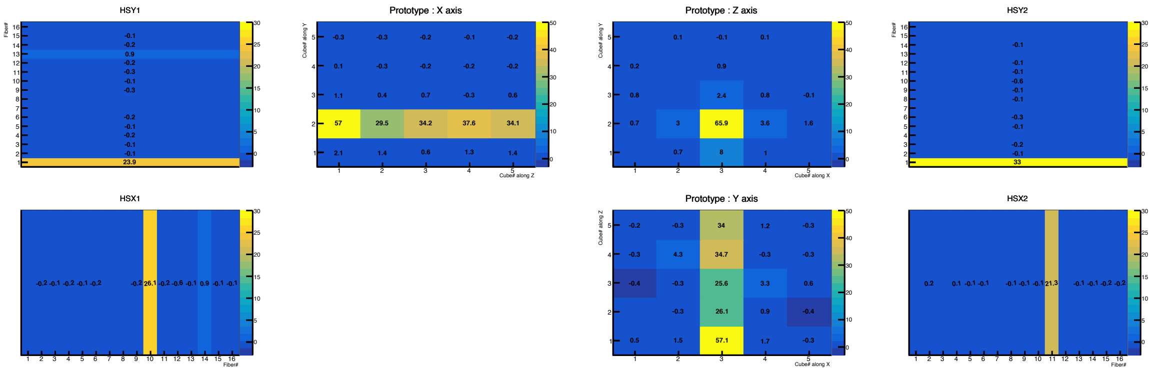

(a) Initial position

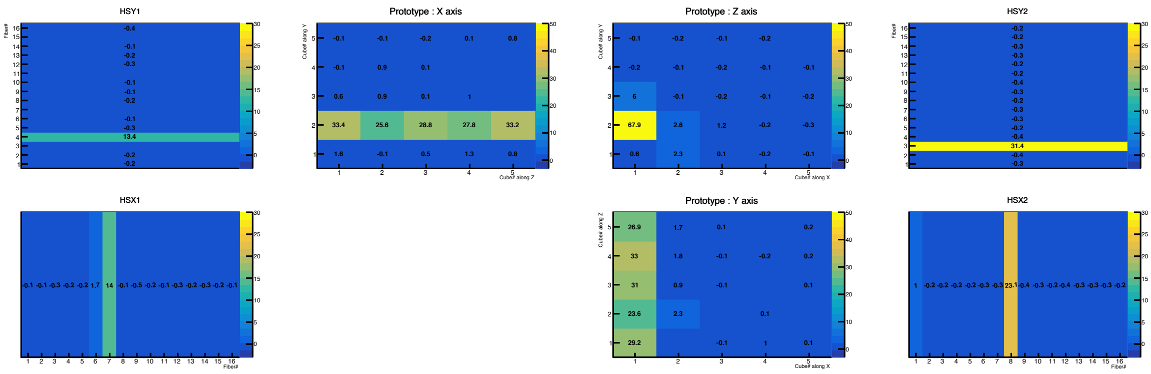

(b) +15mm parallel shift

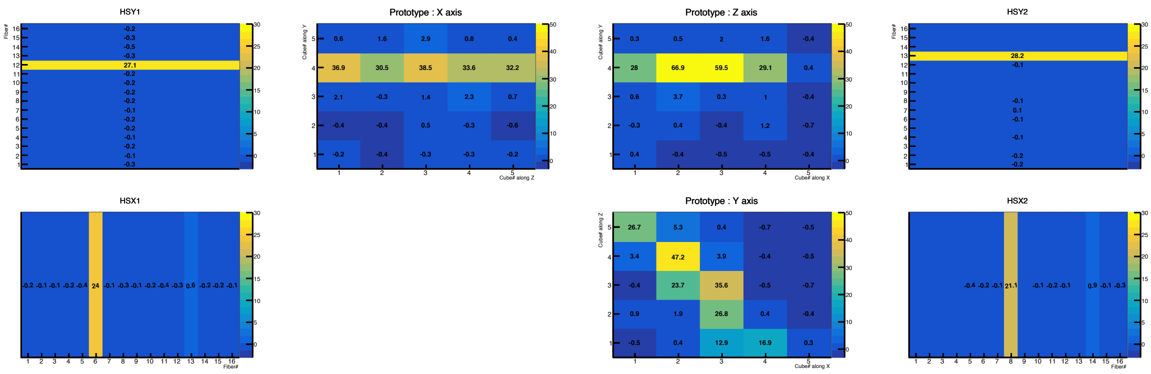

(c) 30° rotation

Figure 3.28: Examples of event display

Figure 3.29 show the light yield distribution of a central channel in each readout direction for the 5×5×5-cube prototype. In the measurement for the prototype, two types of the trigger configuration were used. The run with the trigger configuration using only the upstream hodoscope was used in this result because this trigger configuration made it easy to accept the beam in all scintillator cubes. Moreover, the events with coincident hits in any front and back 5×5 cubes were selected in the analysis. On the other hand, these distributions had pedestal events because this configuration allowed to record the events with hits out of a focused cube. Observed PE in Z direction was saturated around 70 p.e. due to parallelity between the beamline and the Z readout fibers. The definition of observed light yield was the same as described in section 3.4.1. About 30 p.e. of light yield was observed in each readout direction. The lower plot is the distribution of observed light yield for X and Y channels. The ratio of RMS to mean for both readout directions are less than 10%, which was consistent with the result of the optical interface test. The other parameters which could increase the light yield variation were reduced at about 3%, for example the overvoltage to the MPPCs, the difference of fiber length in each optical interface or curvature of the fibers.

Moreover, observed light yield of the central X and Y channels, which correspond to the channel used in the single cube measurement, were 29.0 p.e. and 25.5 p.e., respectively. The difference of light yield in each readout channel between the prototype measurement and the single cube measurement is about 1%. It is suggested that there is no light yield difference depending on the number of adjacent scintillator cubes.

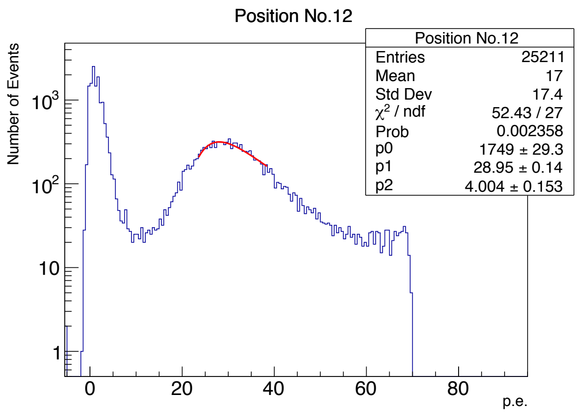

(a) Central X readout

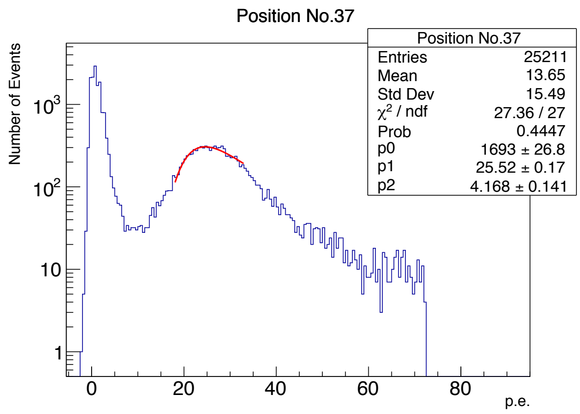

(b) Central Y readout

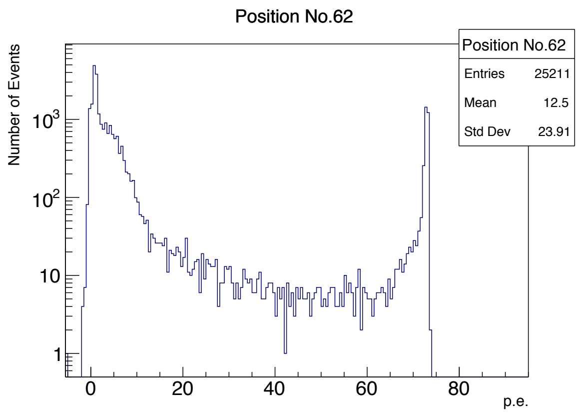

(c) Central Z readout

Figure 3.29: Observed light yield distribution in each readout channel

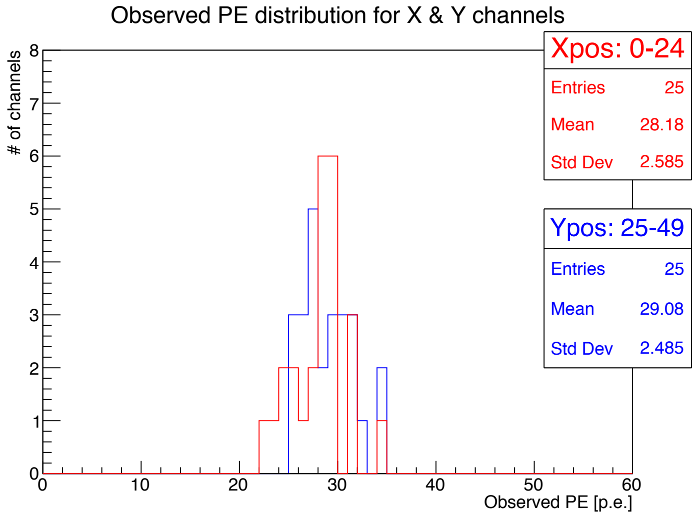

(a) Observed light yield variation for X & Y channels

When the 5×5×5-cube prototype is rotated around the Y axis at an angle, path lengths of the beam in inner 3×3×3 cubes become longer compared to the non-rotated configuration as shown in Fig.3.31. Therefore, light yield for inner 9 channels with an angle rotation is considered to become higher than that with the 0° configuration.

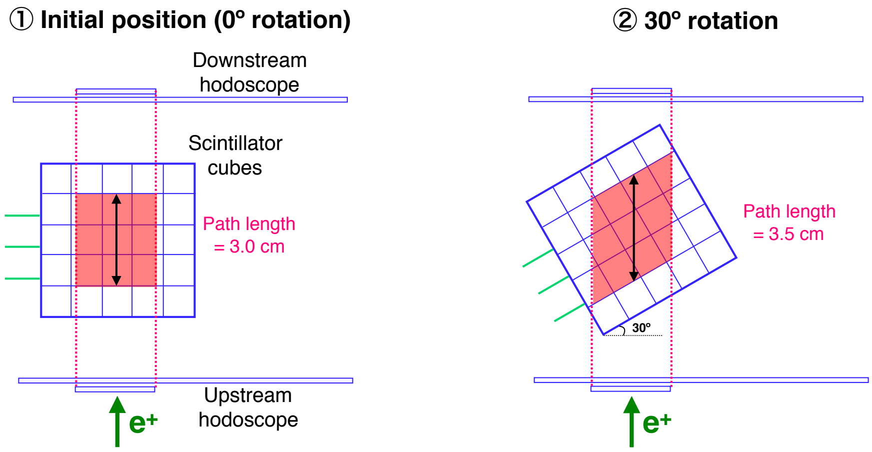

Figure 3.31: Top view of the 5×5×5-cube prototype in each rotation angle. The configuration with 30° rotation has longer path length of the positron beam in the inner 3×3×3 cubes than that with initial position.

The distributions of total light yield for inner 3 readout channels in the X direction are shown in Fig.3.32. These results used the events which passed through the three rows on the same horizontal level in the inner 3×3×3 cubes. Total light yield was also defined as MPV of a fitted landau function. No increase from 0° to 15° was observed, while about 10% increase of total light yield was observed in the configuration with 30° rotation as expected. This difference is comparable considering the range of each uncertainty because the ratio of both path lengths is $\cos 30° \simeq 0.87$. One of the causes of no increase of total light yield in the 15° rotated configuration is considered that the about 3% difference ($\cos 15° \simeq 0.97$) of path length is not so sufficient to observe the light yield difference.

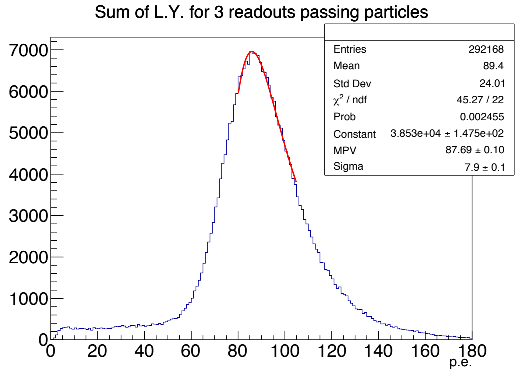

(a) Initial position. Light yield distributed in less than 50 p.e. was considered to be caused by the particle which passed through the gap between the cubes.

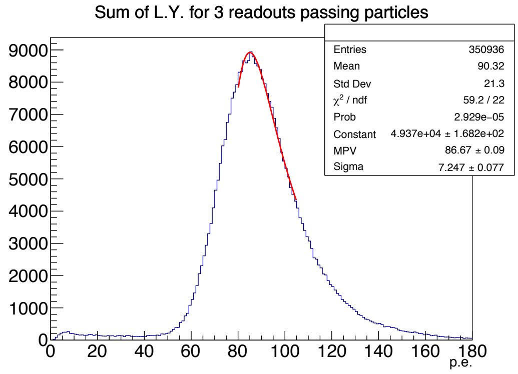

(b) 15° rotation

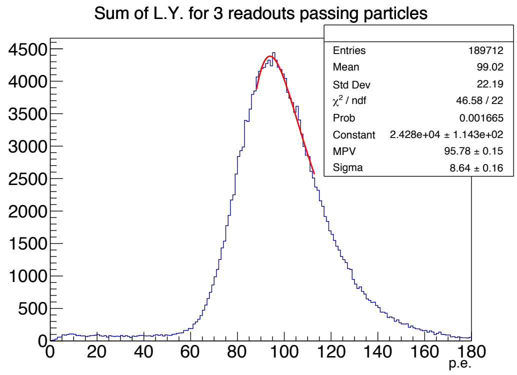

(c) 30° rotation

Configuration	Total light yield [p.e.]
Initial position (0°)	87.7
15° rotation	86.7
30° rotation	95.8

(d) List of total light yield

Figure 3.32: The distributions of total light yield for inner 3 readout channels in the X direction

Observed light yield per MIP in this measurement was about 30 p.e. in each channel, while that in the cosmic-ray test of the extruded cubes with the optical interface was about 70 p.e. as shown in section 2.2.5. The difference between the two values mainly derives from the number of inserted fibers, fiber length and PDE of MPPCs which has positive relation with bias voltage. In the past cosmic-ray test with an extruded cube, it was confirmed that light yield was reduced about 20% every inserted fiber into a cube. Reduction due to attenuation length of the WLS fiber is about 90% (several cm vs. about 30 cm in average). Reduction due to PDE is also about 90% (over voltage of 5 V vs. about 4.5 V). In total, about 48% reduction of light yield was estimated comparing this result with that of the interface test. The other considerable cause is the reduction due to the difference between the average track length of cosmic muons and the positron beam. The beam passed almost along Z direction, while cosmic muons passed through a cube with angles and the average of its track length was longer than the 1 cm cube width. From these considerations, the light yield measured in this beam test is a comparable value to that of the interface test with cosmic-ray.

Chapter 4

Summary and future prospects

4.1 Summary

In the T2K experiment, in order to reduce the systematic uncertainty down to ∼4%, the near detector upgrade project is undertaken. Super-FGD is a new highly granular scintillator target, which will be one of the upgrade detectors added to the upstream part of the current ND280. Super-FGD has the efficient tracking of charged particles and a full poler angle acceptance thanks to its high granularity and three dimensional readouts. The R&D of the Super-FGD components is ongoing by several working groups. We evaluated the optical performance of the scintillator cubes with the optical interface using the positron beam.

In the beam test described in the previous chapter, light yield of at least 20 p.e. per readout fiber from the injected cubes was observed and no reduction of observed light yield and no increase of optical crosstalk was confirmed from extruded cubes to injected ones. From these results, no deterioration of performance is suggested in the real Super-FGD with injected scintillator cubes.

Non-uniformity of optical response from single cube was checked. This result can be useful input for the Monte Carlo simulation of the detector. Better understanding of optical response in single cube could allow to reconstruct and identify charged particles with their momentum and angle more precisely.

The measurement with polystyrene sheets welded onto extruded scintillator cubes was also performed and it was confirmed that the welding method gave no optical disadvantage to the cubes directly. The same result is considered to be obtained even with injected cubes because the method to make a reflector layer on a surface of a scintillator cube is in common between extruded cubes and injected ones. This result will allow to continue the R&D of the cube assembly with ultrasonic welding as one of the feasible method.

Total optical crosstalk rate to 6 adjacent cubes was estimated to about 20% with the injected cubes. However, contact level between two adjacent cubes was not checked quantitively. If crosstalk is affected by pressure to scintillator cubes, that information can be also useful for the simulation because the real Super-FGD is compressed by the box.

The light yield variation with the optical interfaces was observed at less than 10% in the X and Y readout channels with the $5\times5\times5$-cube prototype. This value is consistent with the result of the cosmic-ray test and shows the characteristic of each cube array and connection part in the interface. This result confirmed the performance of the optical interface.

4.2 Future prospects

We confirmed several characteristics of the Super-FGD components with the beam test. The results suggested the feasibility of the full Super-FGD. Moreover, the simulation studies with the new parameters which we have measured can estimate the effects to the physics performance of Super-FGD. On the other hand, new tasks were found to be completed in preparation for the real Super-FGD.

In the beam test, we did not monitor pressure to the scintillator cubes. The scintillator cubes in the real Super-FGD are compressed by the box panels. Therefore, the measurement with controlled pressure needs to be performed. In particular, it should be measured whether optical crosstalk depends on pressure or not because thickness of reflector layers of the cubes seems to be changed by it.

Light emission from the WLS fibers was estimated qualitatively from the external part to the cube. Light yield is expected to be changed by a path length of a charged particle in the fiber. A check of this effect is desired because light emission from the fibers can be one of the parameters for the detector simulations.

Acknowledgment

I would like to express my sincere thanks to my supervisor, Prof. Masashi Yokoyama. He offered many opportunities to gain great experience and practical advice. I also wish to express my appreciation to Tsunayuki Matsubara, who will be promoted to an assistant professor of KEK. Thanks to his tremendous cooperation, I have made a productive research for T2K ND Upgrade. Konosuke Iwamoto, who is a postdoc in Aihara/Yokoyama group in the University of Tokyo, gave me useful suggestions especially in regards to software and helpful support to perform the beam test. Yury Kudenko provided us the scintillator cubes and Davide Sgalaberna provided the optical interfaces including fiber connectors. Without their offers, we could not start to study for Super-FGD.

I owe a debt of gratitude to Dr. Tatsuya Kikawa, Takuji Arihara, Yuito Awataguchi, Soichiro Kuribayshi, Kohei Matsushita for great support in the beam test. I also would like to thank the members in ELPH including Manabu Miyabe who willingly assigned the sufficient beam time to us. I am deeply grateful to Yosuke Ashida, Naruhiro Chikuma, Ayami Hiramoto, Ken'ichi Kin, Naoya Kukita, Riku Tamura, Shin'ya Tanaka, Kenji Yasutome. I have spent my fruitful research life in Tokai. I also appreciate the other colleagues in the T2K experiment and T2K ND Upgrade, and the members in Aihara/Yokoyama group for completion of this study.

Appendix A

Dependence for light yield on the number of inserted fibers

A.1 Motivation

In R&D for Super-FGD, light yield from a scintillator cube is observed for several purposes. Setups for the measurements should be changed according to focused characteristics. Dependence for light yield on the number of inserted fibers to a scintillator cube can be useful information for a quantitive comparison of light yield between different setups. Before the results of the beam test are described, we will report this dependence.

A.2 Experimental setup

Figure A.1 and A.2 show the schematic and pictures of the measurement system for a cosmic-ray test. The system except for NIM modules was placed inside a $50\times50\times50$ cm^3 frame covered with black sheets. Five scintillator cubes produced by extrusion were aligned on the box floor vertically. They were fixed with polystyrene plates and rubber bands. Five WLS fibers were inserted to each cubes and glued by optical cement to a fiber cookie, which was designed for the WAGASCI detector[17]. Each fiber length was about 60 cm. A 32ch-arrayed MPPC S13360(ES2) was attached to the cookie so that its photosensitive areas were matched to the fibers. A picture and parameters of S13360(ES2) are shown in Fig A.3. Overvoltage was set at about 1.7 V. A PCB for the arrayed MPPC was fixed on an iron plate as well as the cookie. Signals from the MPPC were transmitted to the NIM modules via a flat cable.

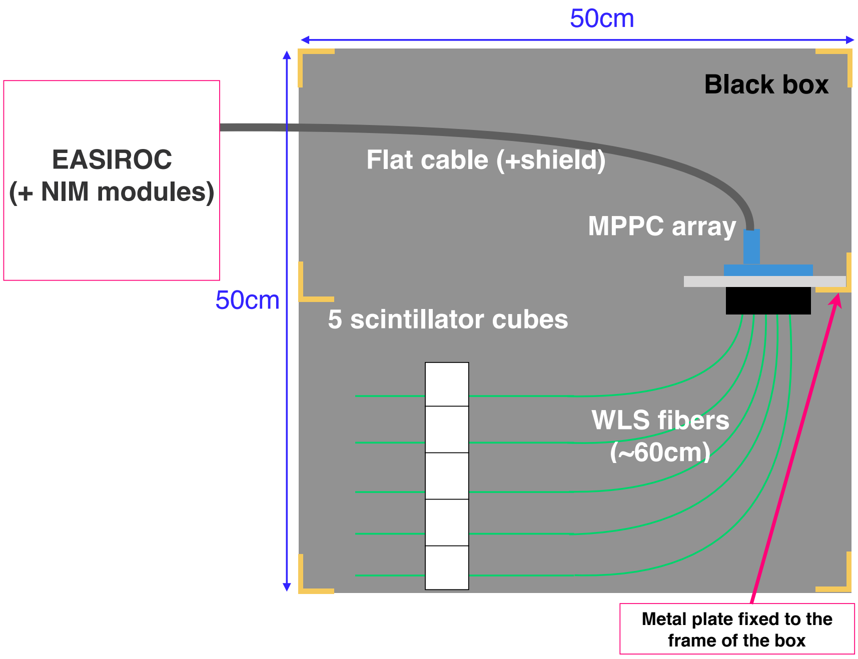

Figure A.1: Schematic of the measurement system for the cosmic-ray test

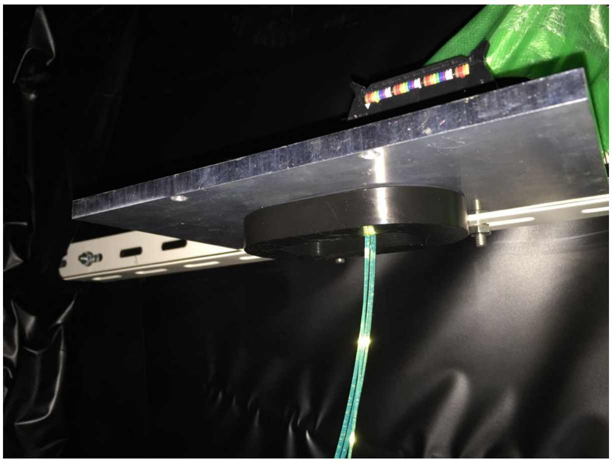

(a) The connection part between a MPPC array and WLS fibers. The fibers were glued into a fiber cookie fixed to an iron plate.

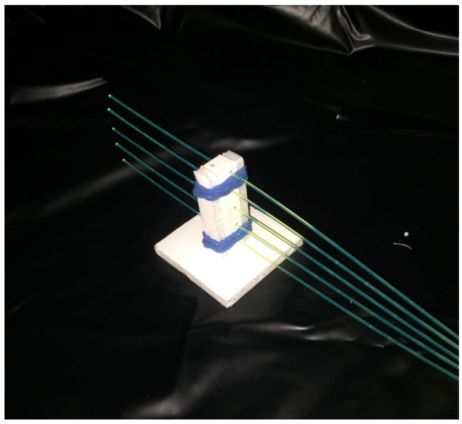

(b) 5 scintillator cubes. They were fixed vertically with polystyrene plates and rubber bands.

Figure A.2: Pictures of the measurement system for the cosmic-ray test

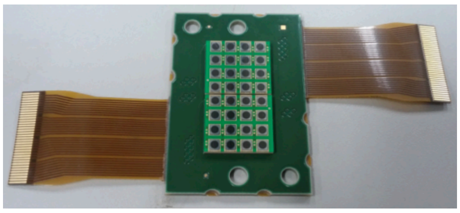

(a) A picture of S13360(ES2)

Item	
Size of a pixel	50 μm
# of pixels	716
Effective photosensitive area	ϕ1.5 mm
Break down voltage	53$\pm$5 V
Typical dark noise rate	60 kHz
Crosstalk rate	3%

(b) Parameters of S13360(ES2)

Figure A.3: S13360(ES2)

Figure A.4 shows the difference between the setups for each number of fibers.The same fiber was used for readout in all setup. In the setups with two and three fibers, non-readout ones were inserted to the rest holes.

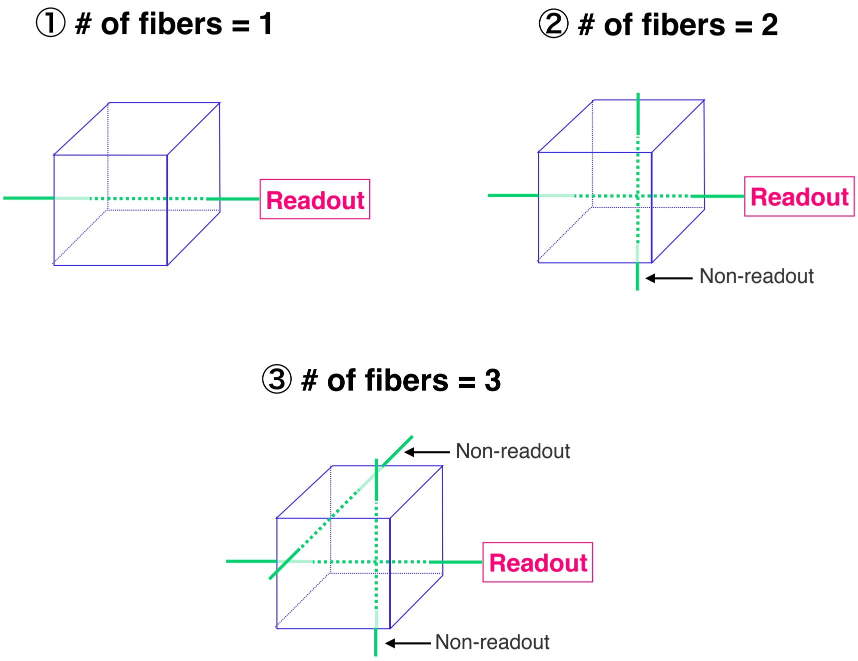

Figure A.4: Difference between the setups for each number of fiber

A.3 Data taking

A NIM EASIROC module was used for the main readout electronics also in this test. The bias voltage to the MPPCs was adjusted in order to equalize a conversion gain for each channel. A definition of the conversion gain is shown in chapter 3.

A typical charge distribution with cosmic-ray data is shown in Fig. A.5. The most left peak corresponds to the pedestal events and the right one next to the pedestal corresponds to the 1 p.e.

level events in each distribution. The peak ADC counts of pedestal and 1 p.e. level are identified as means of each fitted Gaussian function. The gain calibration was performed by the measurement data itself in all five channels.

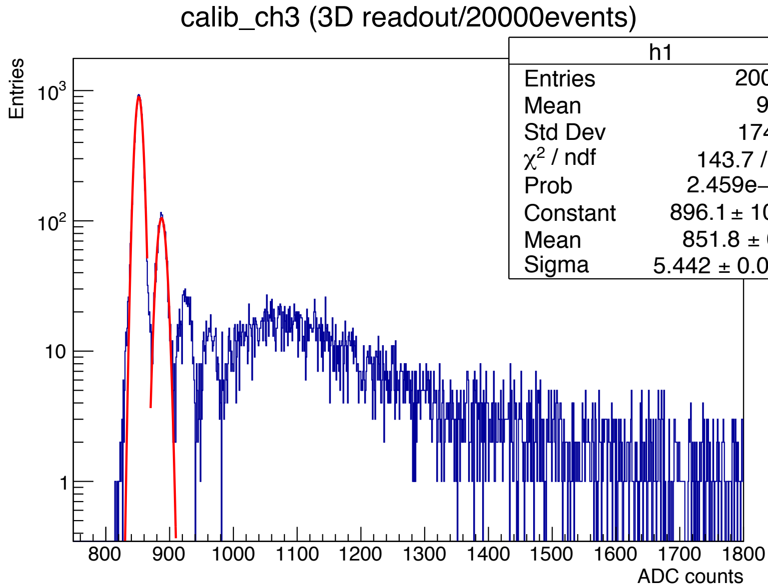

Figure A.5: Typical charge distribution of with the cosmic-ray data. MIP-like event corresponds to the peak around 1100 ADC counts.

The trigger configuration required hits with more than 2.5 p.e. in any channels. Moreover, the events which have two hits in the top and bottom cubes coincidentally were selected in the analysis in order to assure that cosmic muons passed through the three central cubes. The measurement data had 40,000 events in each number of in inserted fibers.

A.4 Results

Figure A.6 show the light yield distribution in each number of inserted fibers. Hits in the central three channels are shown together/; in order to increase statistics. Observed light yield was defined as MPV of a fitted landau function. Observed light yield with one, two and three inserted fiber(s) were 25.3 p.e., 21.2 p.e. and 17.4 p.e., respectively. As shown in Fig.A.7, about 20% reduction of light yield was observed depending on the number of fibers.

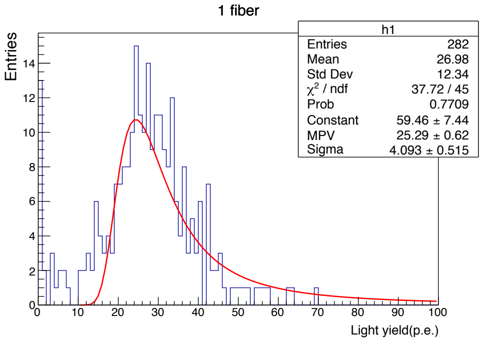

(a) The number of inserted fibers = 1

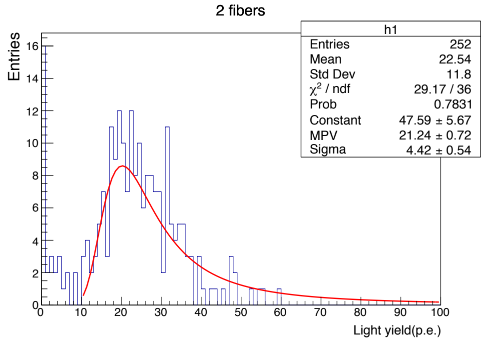

(b) The number of inserted fibers = 2

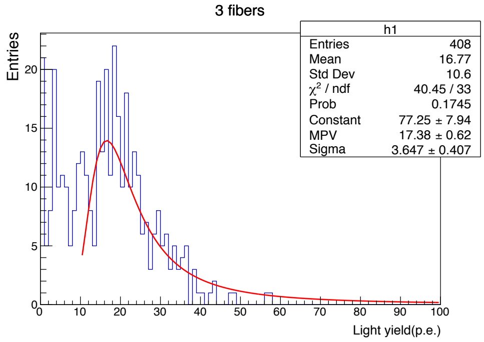

(c) The number of inserted fibers = 3

Figure A.6: Light yield distributions in each n each number of inserted fibers

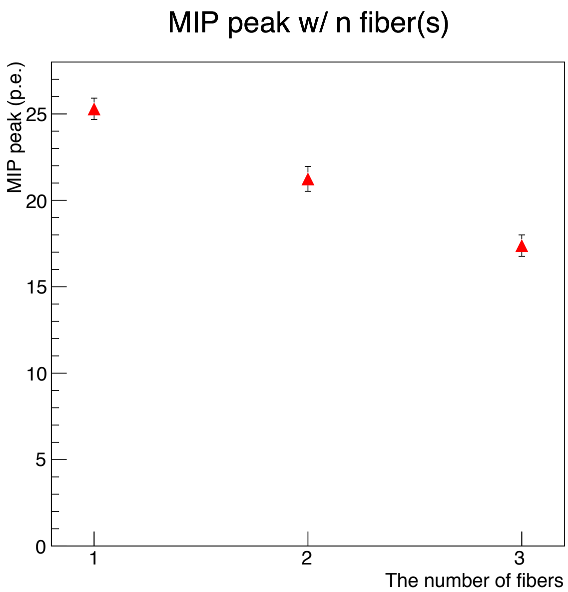

Figure A.7: The graph of observed light yield. The horizontal axis is the number of inserted fibers. Error bars show the MPV error values of each fitted landau function.

Bibliography

[1] Y.Fukuda *et al.* (Super-Kamiokande Collaboration), Phys. Rev. Lett. 81, 1562 (1998)

[2] Y.Hayato, Unification and Development of the Neutrino Science Frontier, https://www-he.scphys.kyoto-u.ac.jp/nufrontier/files/hayato-20140111.pdf

[3] K.Abe *et al.* (T2K Collaboration), The T2K Experiment, Nucl.Instrum.Meth. A659 p. 106-135 (2011)

[4] S.Aoki *et al.* (The NINJA Collaboration), Proposal for precise measurement of neutrino-water cross-section in NINJA physics run, https://j-parc.jp/researcher/Hadron/en/pac_1801/pdf/P71_2018-4.pdf

[5] K. Abe *et al.* (T2K Collaboration), Evidence of electron neutrino appearance in a muon neutrino beam, Phys. Rev. D 88, no. 3, 032002 (2013)

[6] https://www.t2k.org/docs/photos

[7] https://www.ipmu.jp/en/node/1655

[8] K.Abe *et al.* (T2K Collaboration), Proposal for an Extended Run of T2K to 20×10^{21}POT, arXiv:1609.04111 (2016)

[9] A.Blondel *et al.* (T2K Collaboration), The T2K-ND280 upgrade proposal, CERN-SPSC-2018-001 ; SPSC-P-357 (2018)

[10] A.Blondel *et al.* (T2K Collaboration), A fully-active fine-grained detector with three readout views, JINST 13:P02006 (2018)

[11] https://www.hamamatsu.com/jp/ja/product/optical-sensors/mppc/index.html

[12] http://kuraraypsf.jp/psf/

[13] M. Yokoyama *et al.*, Application of Hamamatsu MPPC to T2K Neutrino Detectors, Nucl. Instrum. Meth. A610, 128 (2009), arXiv:0807.3145

[14] F.Moreau, *et al.*, Mass characterization of multi-pixel photon counters for the T2K 280-m near detector, Nucl. Instrum. Meth., vol. A613, p.46-53, (2010)

[15] E.Noah *et al.*, Readout scheme for the Baby-MIND detector, PoS vol. PhotoDet2015, p.031 (2016)

[16] http://omega.in2p3.fr/

[17] B.Quilain, The WAGASCI detector as an off-axis near detector of the T2K and Hyper-Kamiokande experiments, arXiv:1610.06367(2016)

[18] http://www.lns.tohoku.ac.jp/ hadron/beamline.html

[19] http://www.fiberfin.com

[20] I.Nakaura *et al.*, A 64ch readout module for PPD/MPPC/SiPM using EASIROC ASIC, Nucl. Instrum. Meth., vol. A787, p.376-379 (2015)

[21] Amaudruz P.A. *et al.* (T2K ND280 FGD Collaboration), The T2K Fine-Grained Detectors, Nucl.Instrum.Meth. A696 p.1-31 (2012), arXiv:1204.3666